Colors for figures : For a proper readability of the figures, all require color printing.

Graphical Abstract

Designing porous C/C composites for oxidation resistance with an analytical model based on the kinetic and architectural features of fibers and matrix⋆

Marina Fradin, Guillaume Couégnat, Francis Rebillat, Kévin Haras, Gérard L. Vignoles

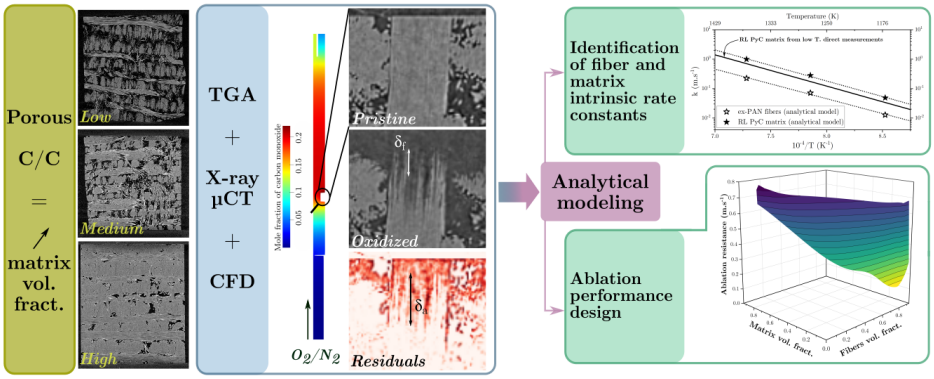

Highlights

Designing porous C/C composites for oxidation resistance with an analytical model based on the kinetic and architectural features of fibers and matrix

Marina Fradin, Guillaume Couégnat, Francis Rebillat, Kévin Haras, Gérard L. Vignoles

- analytical modeling of the oxidation behavior of a porous 3D C/C composite;
- oxidation of C/C composites creates a double affected zone (fiber, matrix);
- affected lengths and areas determined via µCT images and 3D-correlation technique;
- identification of ex-PAN fibers and RL PyC matrix oxidation kinetics in dry air;
- parameters optima for effective reactivity and affected depths are neatly different.

Designing porous C/C composites for oxidation resistance with an analytical model based on the kinetic and architectural features of fibers and matrix

Marina Fradin[a,b,*], Guillaume Couégnat[a], Francis Rebillat[a], Kévin Haras[b], Gérard L. Vignoles[a]

[a] *Laboratoire des Composites ThermoStructuraux (LCTS), UMR 5801 CNRS-Safran-CEA-Université de Bordeaux, 3 Allée de La Boétie, 33600 Pessac, France*
[b] *ArianeGroup SAS, 3 Rue de Touban, 33185 Le Haillan, France*

Abstract

Carbon/Carbon composites used in rocket propulsion contain many process-related pores and have a porosity-dependent oxidation recession rate. A 1D analytical model has been developed to describe this behavior and assess the structure-reactivity relationship for the oxidation of such composites. The model has been compared to experiments for validation. Oxidation experiments have been carried out using samples featuring individually different matrix fractions in a thermogravimetric analysis apparatus under dry air. Post-test morphologies were characterized with X-ray micro-computerized tomography and a 3D-image correlation technique. Finally, guidelines are given for the design and optimization of porous C/C composites with respect to oxidation resistance.

Keywords: A. Carbon/Carbon Composites (CCCs), B. Porosity, C. Analytical modelling, B. Environmental degradation, Design.

1. Introduction

Carbon/Carbon (C/C) composites are widely used for their thermomechanical high resistance properties in various applications: heat exchangers, aircraft

*Working document - not for public release.
*Corresponding author. Tel: (+33) 5 56 84 33 03.
Email address: fradin@lcts.u-bordeaux.fr (Marina Fradin)

brake discs, thermal protective systems for atmospheric re-entry vehicles, solid and liquid rocket motor (SRM/SLM) nozzle throats and divergents [1, 2, 3, 4]. In these applications, physicochemical conditions are harsh and coupled (high pressure and gas velocity, very high temperatures, oxidizing atmospheres, abrasion by solid particles). As carbon is known to begin degrading under dioxygen at temperatures above 673K at atmospheric pressure [5, 6], C/C materials experience oxidation [7] and/or sublimation [8] phenomena, in addition to mechanical etching, leading to material recession [9]. In such applications, especially those related to aerospace technology, predicting material recession under specified conditions is essential. Indeed, this quantity is a first order parameter for SRM design: the dimensional changes of the nozzle diameter induce a loss of engine efficiency [10].

In the past two decades, the behavior of C/C materials under ablation by chemical etching has been experimentally studied and modeled under various conditions. Lachaud *et al.* [11] considered an ideal fully densified 3D C/C composite oxidized in a cylindrical reactor at 898K under dry air at atmospheric pressure. Based on the observation of the surface roughness features, they developed a modeling strategy to predict material behavior from that of its components (*i.e.* fibers, interphase and matrix). The main controlling parameters were found to be the contrasts between the reactivities of the various constituents and the competition between surface reaction and diffusion [12]. Indeed, it is well known that the oxidation kinetics of a dense and predominantly sp^2 carbon material depends on its degree of organization [13, 14, 15]. Furthermore, the non-additive property of fibers and matrix intrinsic kinetics was proven, whereas it was only a guesswork until then. Ferguson *et al.* [16] intended the same modeling strategy with a carbon fibers reinforced fully infused resin matrix composite by a numerical method.

On the other hand, work was done on porous carbon materials. Lachaud *et al.* [17] initiated an elementary approach to model the oxidation behavior of carbon

fibers bundles at 893K under dry air at atmospheric pressure in a cylindrical reactor and identified fibers oxidation kinetics. The Thiele modulus, which is commonly used to describe the reaction/diffusion competition in porous catalysts, has been reformulated to quantify the reaction/diffusion competition in the porous volume of carbon fibrous materials. Panerai *et al.* [18] re-operated the method on carbon fibrous preforms in an air-flow tube under various temperatures and oxygen partial pressures to assess reaction- or diffusion-limited regimes in atmospheric re-entry, via the Thiele modulus analysis. Later, Ferguson *et al.* [16, 19] reconsidered the preliminary strategy with the help of X-ray micro-tomography (µCT) images and a computational framework, assuming the oxygen content in the atmosphere. Vignoles *et al.* [20] went further, considering carbon fibrous preforms nitridation combined with simultaneous nitrogen recombination in a nitrogen plasma atmosphere. They also compared 3D image-based detailed computations to analytical results.

Summarizing, the above-mentioned studies spotlighted the leading and coupled roles of phases reactivity contrasts and surface/volume reaction-to-diffusion rates. However, as they were either modeling fully solid multi-phase materials (fibers/interphase/matrix without pores) or porous materials with a single solid phase, they are not suitable for C/C materials containing porosity. Indeed, their preferred manufacturing process is Chemical Vapor Infiltration (CVI), which is a gas-route densification process of fibrous architectures; it is known to lead to multi-scale porosity and density gradients in parts [1, 21, 22, 23, 24, 25]. Porous C/C composites are three-phase materials (fibers/matrix/pores); therefore, former models of C/C behavior to oxidation are not sufficient in that case. Improving the knowledge of the interaction of porous C/C with their environment is then essential. To address this, the present work is focusing on their physicochemical ablation by oxidation and on identifying the key parameters allowing the most suitable description of their behavior. The central tool of this approach is an analytical model based on previous work [20] and extended to porous materials containing two distinct solid phases. Validation of this model

is sought by comparing its predictions to actual experimental data.

The primary intention here is to provide a methodological framework for the establishment of structure-reactivity relationship in the oxidation process of porous C/C composites and for the quantitative assessment of this reactivity as a function of the matrix volume fraction. However, working immediately with nominal conditions of use (*i.e.* high temperatures, high fluxes, high gas flows, presence of radicals), and materials (almost dense C/C composites) is an additional difficulty in fulfilling these goals. We propose instead to operate in milder conditions, *i.e.* in a ThermoGravimetric Analysis (TGA) apparatus with moderate flows of dry air and temperatures, and with materials displaying a broader porosity range than the operational materials. At very low temperatures, *i.e.* at the onset of carbon oxidation, such an approach would be unnecessary because the very low oxidation rate ensures that carbon mass loss is fully controlled by the chemical reaction itself, but at higher temperatures diffusion effects are expected to take place, either externally or inside the porous material. This is precisely these phenomena that we aim to account for in order to describe correctly the dynamics of material degradation. Once such a framework has been set, it will be possible to extend its application to more realistic ablation cases.

The paper is organized as follows. First, the oxidation of C/C composites with varying matrix volume fractions in a TGA apparatus is characterized and quantified. Then, the model is built and its main analytical results are presented. The third part addresses the exploitation and interpretation of the experimental results with the help of the model. A computational reconstitution of the oxidation experiments is carried out in order to retrieve the environmental conditions at the boundary. Matching trends and values between analytical laws and experimental data are assessed in order to attest of the consistency of the developed approach for varying matrix volume fractions and temperatures. Intrinsic reactivities of the two distinct solid phases are also identified and compared to literature in order to provide a second validation of the whole approach. The last section is devoted to design considerations, featuring in particular a sensiv-

ity analysis on materials parameters with respect to the oxidation behavior and to its potential impact in the whole ablative process.

2. Experimental characterization of C/C composites oxidation

A complete experimental campaign has been carried out on C/C composites with different initial porosities in order to retrieve kinetic and morphological data that will be exploited throughout the analytical modeling process. This campaign is composed of: *(i)* pre-test textural and morphological characterizations ; *(ii)* oxidation tests in a TGA device ; *(iii)* post-test morphological characterizations.

2.1. Materials and methods

2.1.1. Materials

Partly infiltrated 3D needle-punched C/C composites were investigated in this study. The preform is made of carbon yarn sheets of ex-PAN fibers, horizontally and perpendicularly stacked (X, Y plane) and needle-punched in the transverse direction (Z) to hold them together as illustrated on Fig. 1. The fabrication process of the ex-PAN fibers is conventional, as described in the work of Frank *et al.* [26]. Fibers diameter is about 7 µm, their density is equal to 1.8 g.cm^{-3} and their volume fraction in the preform is estimated at 28% [27, 28].

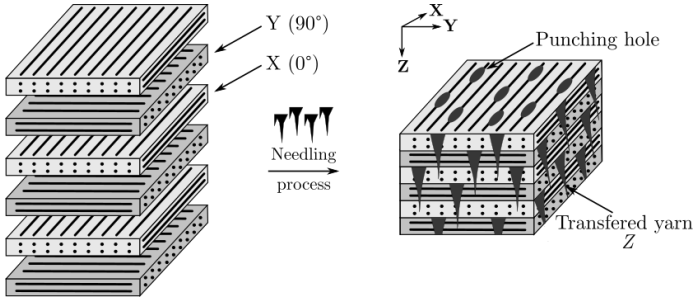

Figure 1: Schematic illustration of the 3D needle-punched C/C architecture.

The Isobaric and Isothermal CVI process (I-CVI) was used to fill the preform with a pyrocarbon (PyC) matrix. Various densification durations were performed to obtain samples displaying different matrix fractions (*i.e.* mass densities). The densified materials have not undergone any thermal treatment after processing.

Fibers and matrix pyrolytic texture and structure features were determined by two complementary methods. First, by measuring the extinction angle (A_e) with an optical microscope Nikon ME600L equipped with a graduated polarizer and an analyzer, using the Polarized Light Optical Microscopy (PLOM) method established by Gillard *et al.* [29]. Then, by assessing the Full Width at Half Maximum of the D-band ($FWHM_D$), the Half Width at Half Maximum of the G-band ($HWHM_G$) and the ratio of the D-band intensity to the G-band intensity (I_D/I_G) on a Raman spectrum, providing details about the amount of graphite edge plane defects and graphitization degree of the different carbonaceous phases [30, 31, 32]. These data were obtained with a LabRAM HR Raman spectrometer using a wave length of 632.8 nm. An attempt to numerically approximate matrix structure descriptors such as the in-plane coherence length (L_a) was undertaken using the method established by Mallet-Ladeira *et al.* [33] based on the $HWHM_G$ parameter. Table 1 sums up texture and structure data for fibers and matrix phases. Fibers displayed a characteristic isotropic texture of ex-PAN fibers [34]. Coupled data from PLOM and Raman indicates that the matrix is made of Rough Laminar (RL) PyC [29]. $FWHM_D$ data implies that matrix graphitic planes contain a larger amount of defects than fibers ones.

Constituant	$\boldsymbol{A_e}$	$\boldsymbol{FWHM_D}$	$\boldsymbol{HWHM_G}$	$\boldsymbol{I_D/I_G}$	$\boldsymbol{L_a}$ [33]
	°	cm^{-1}	cm^{-1}	-	nm
Fibers	0.9 ± 0.6	70.8 ± 2.7	24.9 ± 1.2	4.1 ± 1.5	8.3 ± 0.3
Matrix	14.0 ± 0.7	95.5 ± 6.6	32.1 ± 1.1	3.8 ± 1.2	6.9 ± 0.2

Table 1: Fibers and matrix micro-textural and micro-structural parameters obtained from PLOM technique and Raman spectroscopy.

For oxidation tests, cubic C/C samples of 6 mm edge length were used. After, having been cut off with a wire saw, faces were polished on silicon carbide grit disks. Three separate densities have been tested under three different high temperatures, for a total of five different samples. Table 2 gives details on samples designation, initial mass density, porosity and matrix volume fraction, as well as operating conditions. Mass densities and porosities data were measured with a Micromeritics AccuPyc 1340-1 helium pycnometer. Further details on the pores diameter distribution of the three types of materials are given in Appendix B. The matrix volume fraction is inferred from porosity and fibers volume fraction. Uncertainties in Tables 1 and 2 are given with a level of confidence of 95%.

Sample	**Matrix fraction**	**Porosity**	**Initial mass density**	**Operating conditions**
	%	%	g.cm^{-3}	K — min
A-55-1000	17 ± 4	55 ± 4	0.88 ± 0.06	1273 — 30
A-37-900	35 ± 3	37 ± 3	1.25 ± 0.03	1173 — 60
A-37-1000	35 ± 3	37 ± 3	1.25 ± 0.03	1273 — 30
A-37-1100	35 ± 3	37 ± 3	1.25 ± 0.03	1373 — 25
A-12-1000	59 ± 3	12 ± 2	1.76 ± 0.03	1273 — 30

Table 2: Samples designation, initial mass density, porosity, matrix solid volume fraction, and operating conditions.

2.1.2. Equipment of the oxidation tests

A SETARAM Setsys 1600 TGA reactor was used to carry out oxidation experiments. The internal diameter of the cylindrical reaction chamber was 17.8 mm and it was surrounded by a cylindrical resistive heater. A diagram of the whole equipment is given Figure 2 and an accurate description has been done by Zancanaro *et al.* [35]. A highly accurate balance, with a precision as high as 10^{-5} g, was positioned at the top of the apparatus to measure sample weight loss during testing. Cubic samples were installed in an airy basket-like crucible made of alumina and platinum connected to the balance. They were oriented in a way that the needle-punched fibers were pointing downwards. Gas flow was injected

from the bottom of the chamber. Heating and cooling steps were carried out under a neutral atmosphere of Ar and a 10 K.min^{-1} rate was used to reach the desired temperature. The oxidation process was carried out under isostatic temperatures. The oxidizing gas mixture was composed of O_2 and N_2 with partial pressures of 20 kPa and 80 kPa respectively. The overall oxidizing gas flow was equal to 2 L.h^{-1}. A thermocouple sensor, located close to the sample, monitored the chamber temperature. The test temperatures were 1173K, 1273K and 1373K. Not all samples had the same operating conditions (temperature and duration). Details are given in Table 2.

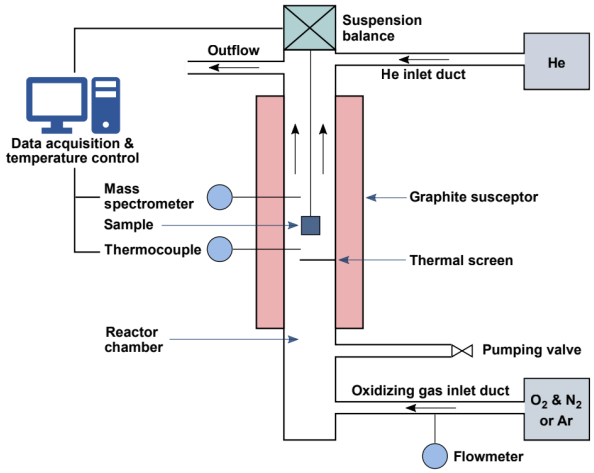

Figure 2: Diagram of the TGA equipment. **color should be used for that figure.**

2.1.3. Characterization techniques

Micrographies of the samples surface were acquired using a Hitachi S4500 FEG Scanning Electron Microscope (SEM).

Morphological alterations of the material, which are affected lengths and depths as well as recession rate, were identified through an innovative approach relying on 3D µCT images correlation. A µCT image of each sample was acquired before and after test with a laboratory tomograph (GE v|tome|x s research edi-

tion, General Electrics, USA). A 100 kV X-ray source with an intensity of 250 µA was used. The exposure time was of 1000 ms and the spatial resolution lied between 4.5 and 5 µm per voxel unit. One acquisition is made of 2000 slices. Images acquired after oxidation (post-test) are registered with respect to their reference state prior to the test (pre-test) with the help of an in-house Digital Volume Correlation (DVC) code, whose methods is detailed in Appendix A. A difference image (residuals) is obtained by subtracting the registered image from the reference one using the *Image Calculator* function in *Fiji* software [36]. The fibers affected length δ_f (µm) is identified on the registered post-test images, the total affected zone length δ_a (µm) on the residues images, and matrix affected length δ_m (µm) is assessed from the substraction of δ_f to δ_a. An affected lengths ratio ξ_i is finally defined as the ratio of δ_f over δ_a, being a dimensionless parameter.

2.1.4. Experimental data processing

According to thermodynamical considerations [37], $CO_{(g)}$ is more likely to be produced than $CO_{2(g)}$ for temperatures above 800K. The reaction equation which is then considered for oxidation tests carried at temperatures equal and above 1173K is the following:

$$2C_{(s)} + O_{2(g)} \rightleftharpoons 2CO_{(g)} \tag{1}$$

The oxidation activity of a C/C composites can be assessed from various methods [38, 39, 40]. Among them, the technique described by Lachaud *et al.* [17] seems to be the most suitable for our study. To use this method, the effective geometric surface of the sample is assumed to remain constant during the oxidation process. The oxidation flux j_{exp} ($\text{g.m}^{-2}\text{.s}^{-1}$) is expressed by Eq. 2 and is calculated from the mass loss rate dm/dt (g.s^{-1}) and the effective geometrical sample surface S_{eff} (m^2). Therefore, j_{exp} is rather associated to an experimental

apparent mass flux.

$$j_{\text{exp}} = -\frac{dm}{dt}.\frac{1}{S_{\text{eff}}} \tag{2}$$

j_{exp} also satisfies Eq. 3:

$$j_{\text{exp}} = \nu_C \; k \; C_{O_2}^{n} \; M_C \tag{3}$$

where ν_C is the carbon stoichiometric factor, k is the reaction rate constant of carbon in dioxygen (m.s^{-1}), C_{O_2} is the dioxygen concentration (mol.m^{-3}), n is the reaction partial order, which is assumed to be equal to 1 under an O_2 atmosphere, in consistency with other previous studies [5, 17, 20]. M_C the carbon molar mass (g.mol^{-1}).

The reaction rate constant k (m.s^{-1}) may be described using the Arrhenius law:

$$k = k_0 \; exp\left(\frac{-E_a}{\mathcal{R}T}\right) \tag{4}$$

where k_0 is the pre-exponential factor (m.s^{-1}), E_a the reaction activation energy (J.mol^{-1}), $\mathcal{R}$ is the universal ideal gas constant (J.mol^{-1}.K^{-1}), and T is the reaction temperature (K).

One can also define an experimental recession rate $\dot{r}_{\text{exp}}$ (µm.s^{-1}) from j_{exp} and ρ_s (g.cm^{-3}) the initial mass density of the material satisfying:

$$\dot{r}_{exp} = \frac{j_{exp}}{\rho_s} \tag{5}$$

In this work, $\dot{r}_{\text{exp}}$ accounts for the experimental recession rate of the exposed composite surface being oxidized in all the complexity of the developed roughness.

2.2. Experimental results

2.2.1. Mass loss rates

The methods described in Section 2.1.4 were used to process oxidation rates from mass loss rates resulting from TGA experiments. Final results for high

temperature tests are given in Table 3. Mass loss and recession rates increase with temperature for A-37 samples of similar matrix fraction due to the kinetic activation. There is not much difference in term of mass loss rates between the samples with different matrix fractions at 1273K.

Sample	j_{exp}	δ_a	ξ_i	$\dot{r}_{exp}$
	$g.m^{-2}.s^{-1}$	µm	-	$µm.s^{-1}$
A-55-1000	0.219	372 ± 33	0.77 ± 0.04	0.25 ± 0.03
A-37-900	0.208	635 ± 83	0.65 ± 0.09	0.16 ± 0.02
A-37-1000	0.224	299 ± 36	0.71 ± 0.08	0.18 ± 0.02
A-37-1100	0.250	168 ± 19	0.69 ± 0.11	0.20 ± 0.02
A-12-1000	0.219	247 ± 25	0.49 ± 0.04	0.12 ± 0.02

Table 3: Mass loss rate and after test morphological characterizations via µCT image correlation.

2.2.2. Morphological alterations

Slices of pre-test, post-test registered and residuals µCT images of sample A-37-1000 are condensed in Fig. 3 as an example. Colors on the image of the residuals (Fig. 3c) indicate areas which underwent oxidation. Very few or almost no trace of oxidation has been reported in the volume at high temperatures. Residuals are intense and concentrated at the sample edge, meaning that oxidation only occurs at its external exposed surface, which is characteristic of an exterior diffusion-limited regime. This observation explains that there is no difference between the mass loss rates with respect to the samples mass density. A focus is made on the surface roughness of sample A-37-1000 on Fig. 4. Fibers are stripped of the matrix. This phenomenon has been extensively discussed in the work of Lachaud *et al.* [11] and indicates that the fibers are more oxidation resistant than the matrix, as the latter recedes sooner and faster due to its higher reactivity to oxidation. Besides, fibers are displaying a needle shape after

oxidation, which has also been demonstrated to be characteristic of a stationary regime in the above-mentioned works. The same observations were made for the other samples through µCT and digital microscope imaging.

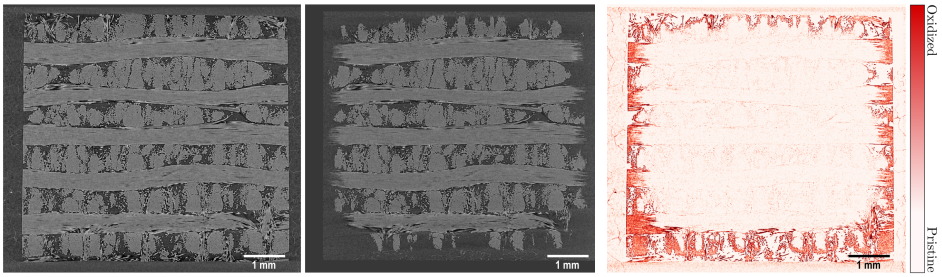

(a) Pre-test (b) Post-test (c) Residuals

Figure 3: Snapshots of the same slice from registered pre- and post-test µCT images and residuals image. **color should be used for that figure.**

The morphological characterization techniques detailed in Section 2.1.3 were used. The detailed values of morphological alterations and uncertainties with a level of confidence of 95% are indicated in Table 3. One can note that the material overall affected length decreases with temperature and with the matrix fraction. On the other hand, the affected lengths ratio slightly increases with temperature and straightly decreases with the matrix fraction. These observations will be discussed in the following sections.

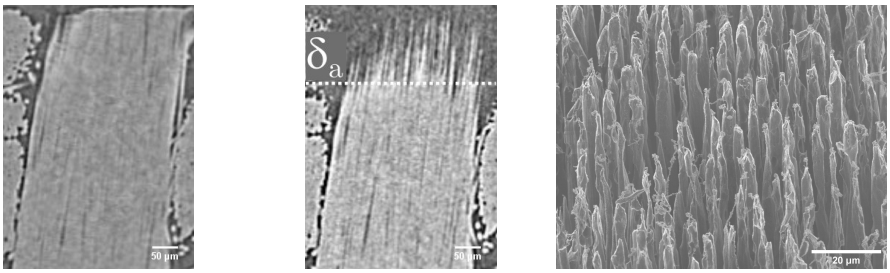

(a) X-ray µCT image before test (b) X-ray µCT image after test (c) SEM image after test

Figure 4: Focus on a yarn tip of sample A-37-1000 on X-ray µCT images (a,b) before and after test and SEM image (c) after test.

3. One-dimensional analytical modeling

The modeling strategy involves the reconstruction of the flow conditions outside the sample surface and the simulation of oxidation inside the sample porous medium. Whereas the former part of the model involves principally classical Computational Fluid Dynamics (CFD) modeling, the latter requires an *ad hoc* treatment, because carbon oxidation, which a heterogeneous chemical reaction, is strongly coupled to the diffusion of dioxygen throughout the porous medium and displays contrasted reaction rates depending on the exposed carbon phase. In many cases, the matrix may be more reactive than the fibers, but the converse situation can be found. There are also cases in which a weak interphase separates fibers and matrix which otherwise have an almost equal reactivity.

In this section, we will propose an extension of a previous analytical model [20] to the case of porous C/C composites containing two solid phases with distinct reactivities. Here, we will focus on a baseline case in which a weaker matrix surrounds stronger fibers, resulting in ablated morphologies exhibiting bare fibers in extreme surface and an affected zone with a certain depth. The model, developed in 1D perpendicularly to the ablated surface, will help connecting the response of the material to oxidation to its morphological and physicochemical parameters.

3.1. Problem description

The proposed model is built at a homogenized scale, *i.e.* the details of the porous medium architecture are not precisely accounted for, but are rather represented by effective quantities, such as the internal surface area and effective diffusion coefficient, given as functions of the volume fractions of matrix and fibers. As only the depth inside the material (x) is considered, the model is uni-dimensional. Heat transfer is not accounted for, considering a uniform temperature in the whole sample. This is justified by the fact that the affected lengths are not large, so that temperature differences between the upper surface and the bottom of the affected zone are small compared to the average temperature. The porous medium is considered initially homogeneous; during oxidation, it will display distributions throughout the depth below the surface of porosity $\varepsilon(x)$, fiber volume fraction $\phi_f(x)$ and matrix volume fraction $\phi_m(x)$, respectively, related to each other through the following equation:

$$\varepsilon(x) = 1 - \phi_f(x) - \phi_m(x) \tag{6}$$

In the case where the matrix is more reactive than the fibers, the affected zone of the material will be split into two zones, one in which some matrix remains and the other one in which the fibers are stripped. Fig. 5 schematizes this situation.

The internal effective surface of the material $\sigma_{v,i}$ ($m^2.m^{-3}$ or m^{-1}), i accounting for fiber or matrix, is essentially the ratio of the specific area ($m^2.g^{-1}$) and the mass density ($g.m^{-3}$) of the material. For fibers and matrix, $\sigma_{v,i}$ is defined by Eqs. 7a and 7b respectively, satisfying:

$$\begin{cases} \sigma_{v,f}(x) = \dfrac{4}{d_f^\star}\sqrt{1-\varepsilon(x)}\sqrt{1-\varepsilon_0} & \text{(7a)} \\ \sigma_{v,m}(x) = \dfrac{4}{d_m^\star}\left(-1 + J\varepsilon(x) + K\varepsilon(x)^2 + L\varepsilon(x)^3 + M\varepsilon(x)^4\right) & \text{(7b)} \end{cases}$$

Eq. 7a stems from the geometrical model of perfect dilute cylinders, which applies correctly to raw fibrous arrangements [41, 42], while Eq. 7b was determined

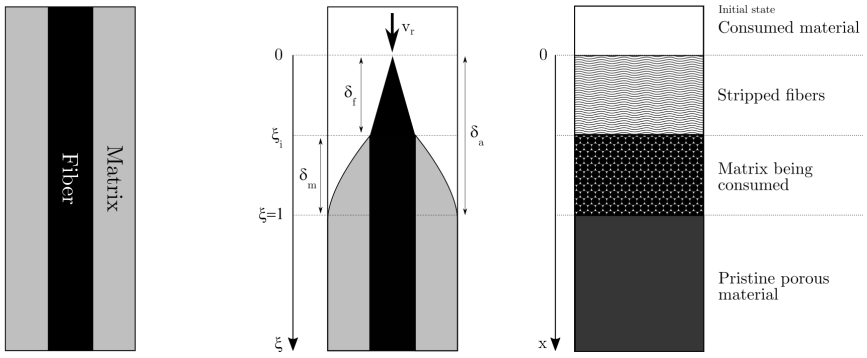

(a) Fiber/matrix system initial state (b) Fiber/matrix system steady oxidation state (c) Overall material steady oxidation state

Figure 5: Scheme of material steady oxidation state: overall and fiber/matrix system focus.

by Charles *et al.* [43] for the C/C material of the present study. Parameters $d_f^\star$, $d_m^\star$, J, K, L and M are given in Table 4.

$\boldsymbol{\sigma_{v,f}(x)}$ **Eq. 7a and** $\boldsymbol{\sigma_{v,m}(x)}$ **Eq. 7b**	
Coefficient	**Values**
$d_f^\star$ (m^{-1})	1.649×10^{-5}
$d_m^\star$ (m^{-1})	1.563×10^{-4}
J (-)	16.822
K (-)	-57.338
L (-)	90.511
M (-)	-53.264

$\boldsymbol{D_p}$ **Eqs. 9 and 10**		
Direction	$\boldsymbol{\eta_{j,lim}}$	$\boldsymbol{\alpha_{b,j}}$
x	1.566	0.559
y	1.227	0.620
z	1.420	0.776
Average on x - y	1.3965	0.5895

Table 4: Parameters for Eqs. 7a and 7b, and Eqs. 9 and 10 respectively.

Thereafter, $\sigma_{v,f}(x)$ and $\sigma_{v,m}(x)$ will be simplified as follows:

$$\begin{cases} \sigma_{v,f}(x) = \dfrac{4}{d_f^\star}\sqrt{\phi_{f,0}}\tilde{\sigma}_{v,f}(x) & \text{(8a)} \\ \sigma_{v,m}(x) = \dfrac{4}{d_m^\star}\tilde{\sigma}_{v,m}(x) & \text{(8b)} \end{cases}$$

where $\tilde{\sigma}_{v,f}(x) = \sqrt{\phi_f(x)}$ and $\tilde{\sigma}_{v,m}(x) = -1 + J\varepsilon(x) + K\varepsilon(x)^2 + L\varepsilon(x)^3 + M\varepsilon(x)^4$. We will also assume that the total internal surface area σ_v is the juxtaposition of the two contributions from fiber and matrix described above.

The effective diffusion coefficient D_p ($\mathrm{m^2.s^{-1}}$), determined by Charles [44], satisfies the following equation:

$$D_p = D_0 \frac{\varepsilon}{\eta_{j,lim}} \left(\frac{\varepsilon - \varepsilon_p}{\varepsilon_{f,0} - \varepsilon_p} \right)^{\alpha_{b,j}} \tag{9}$$

where ε_p and $\varepsilon_{f,0}$ are the percolation and fibrous architecture porosities respectively. $\eta_{j,lim}$ is the medium tortuosity parameter and $\alpha_{b,j}$ is the Archie coefficient, accounted for direction j. These two parameters depend on the fibrous architecture and its direction and are named geometrical diffusion parameters. Their values were determined by Charles [44] and may be found in Table 4. However, in the case of this simplified model, it is possible to keep the following expression without great loss of precision:

$$D_p = D_0 \frac{\varepsilon^{1+\alpha}}{\eta_{lim}} \tag{10}$$

where the parameters α and η_{lim} are averages of $\alpha_{b,j}$ and $\eta_{j,lim}$ respectively on $j = x$ and y. Values are given in Table 4. In the following, the simplified parameter $\gamma = 1 + \alpha$ will be used.

The gas mass balance in the porous medium is the result of a combination of the gas diffusion and the chemical reaction, and satisfies the following equation:

$$\frac{\partial C(x,t)}{\partial t} + \nabla \cdot \Big(-D_p \varepsilon(x,t) \nabla C(x,t) \Big) = -\sigma_v \big(\phi_f(x,t), \phi_m(x,t) \big) k_{het} C(x,t) \tag{11}$$

where k_{het} ($\mathrm{m.s^{-1}}$) is the effective heterogeneous reactivity of the solid phase – be it made of fibers or of matrix – with dioxygen, and C the gaseous species concentration along the porous medium defined for time t and position x. A partial reaction order of 1 is chosen for the reasons detailed in Section 2.1.4.

The solid mass balance in each domain is defined as follows:

$$\begin{cases} -\dfrac{\partial \phi_f(x,t)}{\partial t} = \Omega_{s,f}\sigma_{v,f}\big(\phi_f(x,t)\big)k_{het,f}C(x,t) & \text{(12a)} \\ -\dfrac{\partial \phi_m(x,t)}{\partial t} = \Omega_{s,m}\sigma_{v,m}\big(\phi_m(x,t)\big)k_{het,m}C(x,t) & \text{(12b)} \end{cases}$$

where $\Omega_{s,i} = \frac{M_C}{\rho_{s,i}}$ is the molar volume of the pure solid phase $i \in \{m, f\}$. M_C is the carbon molar mass, equal for carbon fibers and carbon matrix.

The gas mass balance, Eq. 11, combined with 12a and 12b, yields:

$$\frac{\partial C}{\partial t} - \nabla\Big((1-\phi_m-\phi_f)^\gamma \frac{D_0}{\eta_{lim}}\nabla C\Big) - \Omega_{s,m}^{-1}\frac{\partial \phi_m}{\partial t} - \Omega_{s,f}^{-1}\frac{\partial \phi_f}{\partial t} = 0 \tag{13}$$

We are looking for the existence of a steady state regime with a defined recession rate v_r. The analytical solution of the problem is based on the definition of a moving reference frame accompanying the oxidation front. It is detailed in Appendix D.1. The following two sections focus on rearranging the developed expressions in order to fully operate the potential of this model. However, before going further, some parameters set in Appendix D.1, and required in the following sections, have to be introduced here.

First, an explicit definition for the affected lengths ratio ξ_i is:

$$\xi_i = \frac{\delta_f}{\delta_a} \tag{14}$$

Condensation ratios, which are dimensionless parameters, are introduced as:

$$\upsilon_i = C_b\Omega_{s,i} \; i \in \{f; m; c\} \tag{15}$$

where C_b (mol.m^{-3}) is the boundary concentration at the material surface.
The dimensionless Sherwood numbers Sh_i are defined as follows :

$$Sh_i = \frac{k_{het,i}d_i^\star\eta_{lim}}{D_0} \; i \in \{f; m\} \tag{16}$$

The characteristic length ratios λ_i are defined by:

$$\lambda_i = \frac{\delta_a}{d_i^\star} \; i \in \{f; m\} \tag{17}$$

A dimensionless structural parameter Φ_0 linked to gas diffusion appears and is expressed as:

$$\Phi_0 = \phi_{m,0}(1-\phi_{f,0})^{-\gamma} \tag{18}$$

Similarly, another architectural parameter Σ_m linked to the heterogeneous reaction also appears and is not detailed here. This parameter is defined only for $\phi_{f,0}+\phi_{m,0} < 1-\varepsilon_p$. Its expression is not realistic either for too low or too high values of $\phi_{f,0}$ and $\phi_{m,0}$.

3.2. Identification of heterogeneous kinetics

Expressions for $k_{het,f}$ and $k_{het,m}$ are determined as follows:

$$\begin{cases} k_{het,f} = \dfrac{9}{2}\dfrac{D_0}{\Phi_0\eta_{lim}}\dfrac{d_f^\star}{\delta_a^2}\dfrac{1}{\xi_i(4-\frac{5}{2}\xi_i)}\dfrac{\Omega_{s,m}}{\Omega_{s,f}} & \text{(19a)} \\ k_{het,m} = \dfrac{D_0\Sigma_m}{\Phi_0\eta_{lim}}\dfrac{d_m^\star}{\delta_a^2}\dfrac{1}{(1-\xi_i)} & \text{(19b)} \end{cases}$$

See Appendix D.2 for details. Eqs. 19a and 19b only depend on architectural parameters (Φ_0, η_{lim}, $d_f^\star$, Σ_m, $d_m^\star$) and on the lengths δ_a and $\xi_i\delta_a$ affected by oxidation. Therefore, one can identify fibers and matrix heterogeneous kinetics by simply assessing the initial material architectural description and the post-test material morphology.

Eq. 19b can also be recast into the following form:

$$1-\xi_i = \Theta_m^{-2} \tag{20}$$

where Θ_m, called Thiele modulus for the matrix, is equal to $\Theta_m = \delta_a\sqrt{\dfrac{k_{het,m}}{d_m^\star D_0}}\sqrt{\dfrac{\Phi_0\eta_{lim}}{\Sigma_m}}$. Similarly, the Thiele modulus for the fiber is $\Theta_f = \delta_a\sqrt{\dfrac{k_{het,f}}{d_f^\star D_0}}\sqrt{\Phi_0\eta_{lim}}$. These dimensionless parameters quantify the predominance of diffusion or of reaction in the fibers+matrix and the fibers-only domains, respectively. Θ_i lower (*resp.* greater) than 1 means that diffusion (*resp.* reaction) is faster, therefore not controlling.

The reactivity contrast, firstly defined by Lachaud *et al.* [11], is set as $\mathcal{A} = \frac{k_{het,m}}{k_{het,f}} \frac{\Omega_{s,m}}{\Omega_{s,f}}$. The model relates it to the architectural parameters and to the affected lengths ratio:

$$\mathcal{A} = \frac{2}{9} \frac{d_m^\star}{d_f^\star} \Sigma_m \frac{\xi_i(4 - \frac{5}{2}\xi_i)}{(1 - \xi_i)} \tag{21}$$

Strong contrasts ($\mathcal{A} \to 0$ or $\mathcal{A} \to \infty$) are translated by $\xi_i \to 0$ or $\xi_i \to 1$ respectively. For instance, when the fibers are markedly more resistant to oxidation than the matrix, almost all of the affected length contains a fibers-only region. On the other hand, when the contrast is low ($\mathcal{A} \approx 1$), ξ_i is close to $\frac{1}{2}$.

3.3. Predicting post-test morphologies

Making use of some of the set up equations and starting from heterogeneous kinetics and environmental conditions, oxidized morphologies (δ_a, $\delta_a \xi_i$), overall recession rate (v_r) and material efficiency (k_{eff}) may be predicted.

Eqs. 19a and 19b can be rearranged to make δ_a appear explicitly:

$$\frac{1}{\delta_a^2} = \frac{\Phi_0 Sh_m}{5\Sigma_m d_m^{\star 2}} \left(1 - \frac{9}{2} \frac{\mathcal{A}}{\Sigma_m} \frac{d_f^\star}{d_m^\star} + \sqrt{16 - 9\frac{\mathcal{A}}{\Sigma_m} \frac{d_f^\star}{d_m^\star} + \frac{81}{4} \frac{\mathcal{A}^2}{\Sigma_m^2} \frac{d_f^{\star 2}}{d_m^{\star 2}}} \right) \tag{22}$$

Thanks to this relation, an expression for ξ_i as a sole function of the structural parameters and of the reactivity contrast is found:

$$\begin{cases} \xi_i = 1 - \dfrac{1 - W + \sqrt{16 - 2W + W^2}}{5} & \text{(23a)} \\ W = \dfrac{9}{2} \dfrac{\mathcal{F}}{\Sigma_m} & \text{(23b)} \\ \mathcal{F} = \mathcal{A} \dfrac{d_f^\star}{d_m^\star} & \text{(23c)} \end{cases}$$

As a consequence, knowing the architectural definition of the material, the environmental conditions in which it is placed and the heterogeneous kinetics of the two phases, post-test morphologies may be pre-empted thanks to Eqs. 14, 22 and 23. As an example, the evolution of ξ_i with respect to the architectural parameters and for $\mathcal{F}$ equal to 0.1 is given on Fig. D.3 (Appendix D.3).

Making the assumption that $\upsilon_c^{-1} \gg 1$, an analytical relation for the recession rate v_r as a function of ξ_i and δ_a is determined (see Appendix D.4):

$$v_r = \frac{2D_0}{\delta_a \eta_{lim}} \frac{1}{\upsilon_c^{-1}\xi_i + \frac{\Phi_0}{3\upsilon_m}(4-\xi_i)} \tag{24}$$

In practice, v_r is the analytical version of the experimental recession rate $\dot{r}_{exp}$, as soon as a steady state has been reached. Recalling that δ_a and ξ_i are given explicitly by Eqs. 22 and 23a, we now have a prediction of v_r only from the materials parameters and of C_b (see the definitions of υ_c and υ_m). The latter quantity is attained through CFD computations of the flow surrounding the sample, as will be shown later.

The effective oxidation rate of the material is defined as $k_{\text{eff}} = \dfrac{v_r}{\upsilon_c}$ meaning that:

$$\frac{k_{\text{eff}}}{k_{het,m}} = \frac{2}{Sh_m \lambda_m} \frac{1}{\xi_i + \frac{\Phi_0}{3}\frac{\Omega_{s,c}}{\Omega_{s,m}}(4-\xi_i)} \tag{25}$$

All quantities describing the material response are now explicitly defined. Experimental results and analytical modeling will now be confronted.

4. Exploitation of the experimental results and model validation

4.1. Computational reconstitution of the oxidation tests and identification of the environment

The analytical model developed in Section 3 is applicable in steady state. Experimental results from Table 3 satisfy this condition and are to be exploited in order to experience and validate the model. However, before operating it, environmental parameters, such as the boundary concentration C_b and the diffusion coefficient D_0, have to be calculated for each set of oxidizing conditions.

The classical correlation of Massman [45] for binary diffusion coefficients is employed (see Appendix E for details) and the selected D_0 coefficients are summed up in Table 5. The boundary concentration is retrieved through the use of a CFD modeling of the TGA reactor on ANSYS Fluent (Table 5), that aims at reconstructing the oxidizing environment around the sample. The computational

setup and the data processing details are given in Appendix E. Another outcome of the numerical reconsitution of the oxidation tests is the identification of an apparent geometrical surface reactivity of the sample surface k_{app} (m.s^{-1}) (see Appendix E) that verifies Eq. 26 (with $n = 1$). k_{app} values are summed up in Table 5.

$$\frac{dm}{dt} = -j_{\text{exp}}\ S_{\text{eff}} = -k_{\text{app}}\ S_{\text{eff}}\ C_{O_2}^{n}\ M_C \tag{26}$$

Sample	$\boldsymbol{C_b}$ mol.m^{-3}	$\boldsymbol{k_{app}}$ m.s^{-1}	$\boldsymbol{D_0}$ m^2.s^{-1}
A-55-1000	0.20	8.9×10^{-2}	2.3×10^{-4}
A-37-900	0.31	5.6×10^{-2}	2.0×10^{-4}
A-37-1000	0.19	9.9×10^{-2}	2.3×10^{-4}
A-37-1100	0.10	2.0×10^{-1}	2.5×10^{-4}
A-12-1000	0.20	8.9×10^{-2}	2.3×10^{-4}

Table 5: Binary coefficients from Massman [45], boundary concentrations and apparent geometrical reactivities retrieved from the numerical reconstruction.

Fig. 6 displays the reconstructed conditions of temperature, gas velocity, and mole fractions of O_2 and CO for the oxidation test of sample A-37-1000. For reasons of convenience, the experiment is drawn horizontally.

Some interpretations can be made by now. First, for samples A-37, boundary concentration decreases and apparent surface reactivity increases as oxidation temperature goes up. This is the illustration of reaction/diffusion competition: on the one hand, the overall material reactivity increases with temperature, on the other hand diffusion to the sample surface is limited due to the high material chemical reactivity. As the oxidative gas is depleted at the sample surface, a concentration gradient and a diffusion boundary layer occur (Fig. 6c). These results are in accordance with Eq. 25. Noticeably, there are few disparities

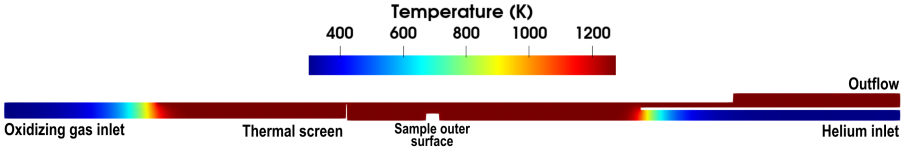

(a) Temperature (K)

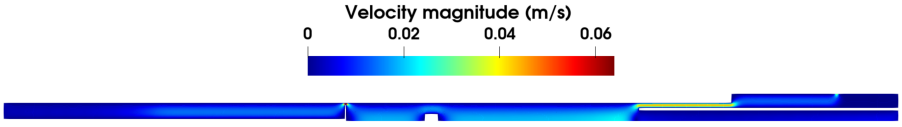

(b) Velocity magnitude (m.s^{-1})

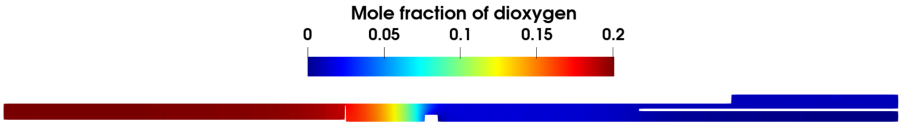

(c) Mole fraction of O_2

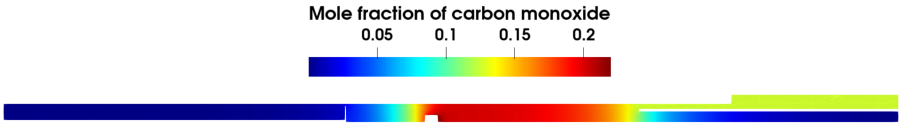

(d) Mole fraction of CO

Figure 6: TGA reactor geometry and experimental conditions for A-37-1000 sample. **color should be used for that figure.**

between the data collected for samples A-55, A-37 and A-12 at 1273K, as they displayed very similar oxidation activities. Marked differences are expected for k_{eff} with respect to the matrix volume fractions when operating the analytical model.

4.2. Interpretations of the experimental results

Initial architectural state ($\phi_{f,0}$, $\phi_{m,0}$, $d_f^\star$, $d_m^\star$, η_{lim}, α), as well as environmental parameters (C_b, D_0), and morphological alterations (δ_a, ξ_i) identified in Sections 2.2 and 4.1 can now be combined in the equations determined in Section 3. The considered solid molar volumes for the fibers and the matrix are of 6.4×10^{-6} m^3.mol^{-1} and 5.7×10^{-6} m^3.mol^{-1} respectively.

4.2.1. Identification of fibers and matrix heterogeneous reactivities

The fibers and matrix heterogeneous kinetics related to the reaction equation Eq. 1 and associated to Eq. 3 are written $k_{het,f}^{CO}$ and $k_{het,m}^{CO}$. They can be identified by means of Eqs. 19a and 19b. One has to consider that $k_{het,f} = \nu_C \; k_{het,f}^{CO}$ and $k_{het,m} = \nu_C \; k_{het,m}^{CO}$, with ν_C equal to 2. The results provided in Table 6 confirm the morphological observations made in Section 2.2 and the amounts of in-plane defects characterized in Section 2.1.1: the matrix is far less oxidation-resistant than the fibers and disappears the earliest. At 1273K, the kinetics values for the fibers and the matrix determined over samples of different porosities are very consistent with each other, with a satisfactory relative margin between 2% to 26%. The reactivity contrast $\mathcal{A}$ and extended reactivity contrast $\mathcal{F}$ have been calculated in each case from the equations given in Sections 3.2 and 3.3. The values of $\mathcal{A}$ above 1 and of $\mathcal{F}$ above 0.1 attest that the material behavior is kinetically controlled by the matrix at any temperatures. Concerning samples A-37, fibers and matrix kinetics logically increase with the temperature, as predicted by the Arrhenius law. However, the reactivity contrasts are not constant, but also slightly increase, meaning that the discrepancy in the oxidation resistance between the fibers and the matrix is enhanced by temperature. The slight rise of ξ_i in Table 3 attests that the relative thickness of the matrix-free affected zone might be enhanced by an increase of temperature.

Sample	$\boldsymbol{k_{het,f}^{CO}}$	$\boldsymbol{k_{het,m}^{CO}}$	$\boldsymbol{\mathcal{A}}$	$\boldsymbol{\mathcal{F}}$	$\boldsymbol{k_{\text{eff}}}$	$\boldsymbol{k_{\text{eff}}}$ / $\boldsymbol{k_{\text{app}}}$	$\boldsymbol{v_r}$	$\boldsymbol{v_r}$ / $\boldsymbol{\dot{r}_{\text{exp}}}$
	m.s^{-1}	m.s^{-1}	-	-	m.s^{-1}	-	µm.s^{-1}	-
A-55-1000	8.6×10^{-2}	2.5×10^{-1}	2.5	0.27	5.9×10^{-1}	6.6	1.64	6.3
A-37-900	1.3×10^{-2}	4.9×10^{-2}	3.4	0.36	2.6×10^{-1}	4.6	0.75	4.7
A-37-1000	6.3×10^{-2}	3.0×10^{-1}	4.2	0.45	6.1×10^{-1}	6.1	1.07	5.9
A-37-1100	2.2×10^{-1}	9.9×10^{-1}	3.9	0.41	1.21	5.9	1.16	5.8
A-12-1000	6.4×10^{-2}	2.9×10^{-1}	4.1	0.44	7.0×10^{-1}	7.8	0.96	8.0
Mean at 1273K	7.1×10^{-2}	2.8×10^{-1}	3.6	0.38	-	-	-	-

Table 6: Kinetics data and material recession rates from analytical calculations and comparison to experimental results and numerical computations.

4.2.2. Affected lengths and ratio

The experimental values of δ_a and ξ_i at 1273K from Table 3 display a straight decrease with respect to the matrix volume fraction. The model-predicted evolutions of δ_a and ξ_i are plotted on Fig. 7 with respect to $\phi_{m,0}$ for $\mathcal{F} = 0.38$, corresponding to the actual averaged reactivity contrast computed in Table 6. Fig. 7 provides a very good fit between the experimental results and the analytical evolutions (for an averaged kinetic situation), within their respective margins.

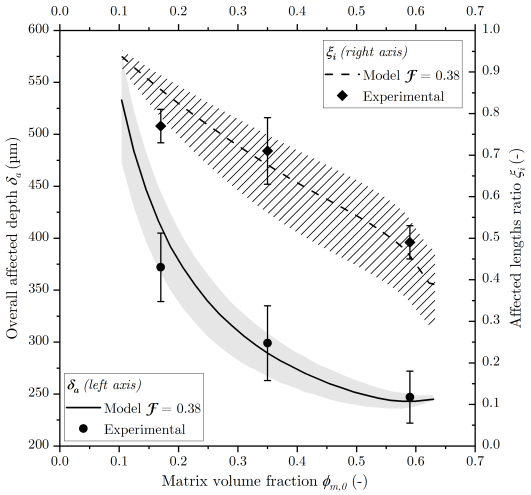

Figure 7: Evolution of the model-predicted values of δ_a and ξ_i with respect to $\phi_{m,0}$ for $\mathcal{F} = 0.38$ and $\phi_{f,0} = 0.28$ and comparison to the experimental results. **color should be used for that figure.**

Relative margins for δ_a and ξ_i between the analytical prediction for $\mathcal{F} = 0.38$ and the experimental results have been computed in Table 7. They reveal slight deviations. The highest deviation for δ_a values, as well as for ξ_i ones, occurs for the sample featuring the lowest matrix fractions. These observations attest of the representativity of the model, especially for relatively high matrix rates.

Sample	Overall affected depth δ_a			Affected lengths ratio ξ_i		
	Experimental	Model $\mathcal{F} = 0.38$	Relative margin	Experimental	Model $\mathcal{F} = 0.38$	Relative margin
	µm	µm	%	-	-	%
A-55-1000	372	417	+12.1	0.77	0.86	+11.8
A-37-1000	299	286	-4.3	0.71	0.67	-5.3
A-12-1000	247	243	-1.6	0.49	0.47	-3.8

Table 7: Relative margins between the model-predicted values of δ_a and ξ_i for $\mathcal{F} = 0.38$ and the experimental results.

On the other hand, in Section 4.2.1, the increase of ξ_i with temperature has been evidenced through the analysis of the experimental data collected and the evolution of the analytically computed values of $\mathcal{A}$ and $\mathcal{F}$. To illustrate this behavior, Fig. 8 represents the evolution of the analytical law of ξ_i with $\mathcal{F}$ (*i.e.* temperature in that case) from Eq. 23a for a material similar to samples A-37. The increase of the affected lengths ratio with $\mathcal{F}$ is in agreement with the above analysis concerning the dependency of ξ_i with respect to the temperature. Besides, one can notice that up to a certain value of $\mathcal{F}$, ξ_i tends to 1, meaning that the fibers are completely stripped of the matrix when the latter is much more reactive.

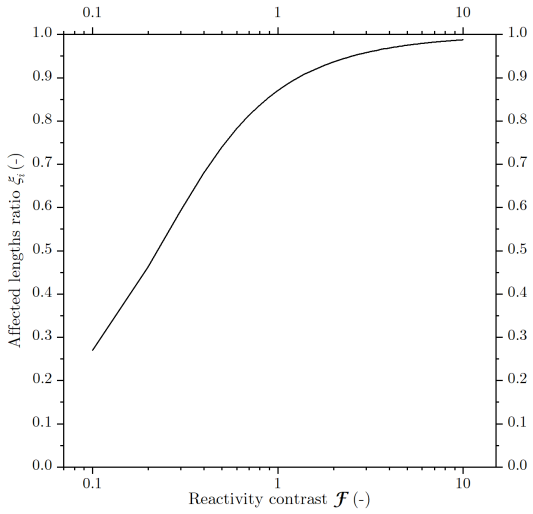

Figure 8: Evolution of ξ_i with $\mathcal{F}$ for $\phi_{f,0} = 0.28$ and $\phi_{m,0} = 0.35$.

4.2.3. Material effective reactivity

As matrix heterogeneous reactivities and extended reactivity contrasts are now identified, analytical values for k_{eff} are determined in Table 6 from Eq. 25. As mentioned above, k_{eff} evolves logically with temperature for samples A-37, as does k_{app}. On the other hand, at 1273K, k_{eff} is calculated for each porous sample and increases with matrix volume fraction. The evolution of k_{eff} in the whole $\{\phi_{f,0}; \phi_{m,0}\}$ parameter space is illustrated on Fig. 9, for $\mathcal{F} = 0.38$ which is the average value of $\mathcal{F}$ at 1273K as suggested in Table 6. It supports the fact that the material effective reactivity is strongly enhanced by the matrix volume fraction in this experimental study. Even though k_{eff} and numerically determined k_{app} differ by a factor 4.6 to 7.8, as indicated in Table 6, the analytical law for k_{eff} has the merit of reproducing the sensitivity of effective reactivity to the different solid fractions.

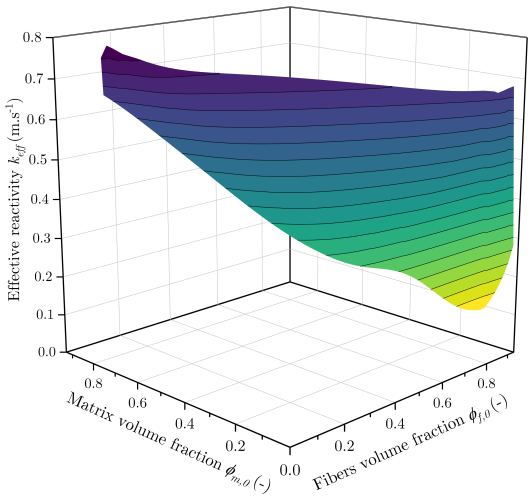

Figure 9: Evolution of the analytical law of k_{eff} at 1273K for $\mathcal{F}$ equal to 0.38 in the $\{\phi_{f,0}; \phi_{m,0}\}$ parameter space. **color should be used for that figure.**

4.2.4. Material recession rate

Architectural features, morphological alterations and environmental parameters are injected in Eq. 24 to compute analytical values for the recession rate v_r. Results are summarized in Table 6. The analytical recession rate increases logically with temperature and decreases with respect to the matrix fraction. A comparison with the experimental data is provided in Table 6. In each case, analytical recession rates differ from the experimental ones with a factor 4.7 to 8.0, as for the numerical and analytical effective reactivities mentioned above. The recession rate is a peculiar parameter compared to others because of its first-order dependence to the boundary concentration, which is numerically determined as detailed in Section 4.1. The apparent recession rate k_{app} defined by Eq. 26 also depends to the first order on C_b, troughout CFD computations. Therefore, the assumption that the concentration is over-estimated by the numerical reconstruction of a factor 4.6 to 8.0 is made. Besides, the very satisfying adequation between analytical law and experimental results for ξ_i, which only depends on architectural and kinetical features, supports this conjecture.

To sum up, the confrontation of the analytical model with the experimental data has attested of its consistency. It has also highlighted the requirement of accurately assessing the boundary concentration of the oxidizing species in case of predicting the recession rate. We will now further appraise its pertinence by comparing the identified heterogeneous kinetics with other studies from literature.

4.3. Comparison of the identified oxidation kinetics to previous studies

4.3.1. Heterogeneous reactivities

Another manner to assess the acceptability of the model is to compare the estimated fibers and matrix heterogeneous kinetic rate constants to other studies. This is made on Fig. 10. The values identified at 1273K for three different porosities are averaged for sake of simplicity, as displayed in Table 6. A focus on temperatures between approximately 900 and 1800K is made. The oxidation

behavior in dry air of various types of carbonaceous materials from petroleum coke to nuclear graphite has been summarized by Smith [5]. Analytically determined heterogeneous kinetics of the fibers and the matrix are indeed located within the scatter bounds of Smith's data, when converted into the units of the present study. Nonetheless, RL PyC matrix data are quite close to the upper bound. Thereafter, for consistency reasons, all data from literature provided below are converted in the units of the present study.

Oxidation kinetic of ex-PAN fibers under air, dry air and pure oxygen atmospheres has been extensively studied in literature. The works of Halbig *et al.* [46] and Govorov *et al.* [47] are selected for comparison because they were carried out on T300 and PANex35 ex-PAN fibers respectively, carbonized at a temperature similar to that of the fibers of this study, and oxidized in TGA devices under pure oxygen. Empty star symbols on Fig. 10, corresponding to $k_{het,f}$, are well located right over the two corresponding curves attesting of the consistency between literature data and the model results.

On the other hand, detailed kinetics data concerning Rough Laminar pyrocarbons oxidized in dry air are missing in literature, as they have never been characterized in that way before. Therefore, data from resin-derived carbons [48] and ex-CVD (Chemical Vapor Deposition) matrix were gathered [49] in order to assess matrix kinetics determined with our model-based data analysis. Bertran [50] indicates a $FWHM_D$ of 133 cm^{-1} for a phenolic resin derived carbon [51]. In their works, Ehrburger *et al.* [15] and Lahaye *et al.* [13] made a strong correlation between carbon defects amount, active sites and reactivity. Thus, on the basis of $FWHM_D$ structural parameter, the PyC matrix of the present study would be more resistant to oxidation than resin derived carbon. This may explain lower kinetics for PyC materials as exposed by Fig. 10. Besides, ex-pitch and coke materials are commonly reported as being less organized than pyrocarbons and feature a higher amount of active sites [15], leading to higher oxidation kinetics. On the other hand, ex-CVD and ex-CVI matrix might be quite similar because of the similarities in the fabrication process. The kinetic evolution corresponding to the ex-CVD matrix are crossing the RL PyC

data as displayed on Fig. 10. Finally, an Arrhenius law has been previously determined for the RL PyC matrix of this study by experimental means in the work of Fradin *et al.* [52]. Oxidation tests were performed on A-37 like samples at low temperatures under dry air in chemical-controlled regime. Experimental data from this work display a very concordant matching with the analytical heterogeneous kinetics (Fig. 10). These fits strengthen the trust in the kinetics values identified via the analytical process for the RL pyrocarbon in dry air. This represents one of the major results of this study.

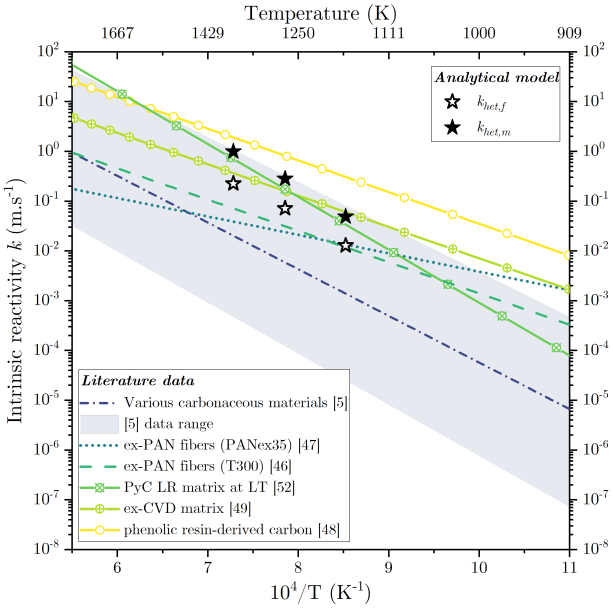

Figure 10: Comparison of analytical modeling results to oxidation kinetics of various carbonaceous materials, ex-PAN fibers and ex-pitch matrix under dry air from literature (LT = low temperatures) [5, 46, 47, 48, 49, 52]. **color should be used for that figure.**

4.3.2. Activation energies

Activation energies are extracted from the analytical heterogeneous kinetics from Fig. 10. A value of 192.4 kJ.mol^{-1} is computed for the fibers and one of 202.2 kJ.mol^{-1} for the matrix. These values are compared to other data from

literature in Table 8 and attest of a good consistency, contributing to validate the model.

Constituant	Reference	E_a $kJ.mol^{-1}$	Carbonaceous material	Atmosphere
Fibers	Dacic and Marinkovic [39]	181	ex-PAN	air
	Lamouroux *et al.* [53]	160 - 200	T300 ex-PAN	pure oxygen
	Zhao *et al.* [54]	191	ex-PAN	air
	This study	192.4	ex-PAN	dry air
Matrix	Dacic and Marinkovic [39]	184	ex-CVD matrix	air
	Ehrburger [15]	130	pyrocarbons	air
	Chang and Rusnak [38]	146 - 181	ground ex-resin C/C	air
	Bertran *et al.* [48]	122	ex-resin matrix	dry air
	Fradin *et al.* [52]	203.2	ex-CVI RL PyC matrix	dry air
	This study	202.2	ex-CVI RL PyC matrix	dry air

Table 8: Activation energy data of various carbonaceaous material under O_2-containing atmospheres.

However, one can notice that the matrix displays a slightly higher activation energy than the fibers, but has been experimentally proven to be less resistant to oxidation. Therefore, pre-exponential factor of Arrhenius law has to be considered as well. In the present study, a pre-exponential factor k_0 of 5.0×10^6 $m.s^{-1}$ has been determined for the fibers whereas it is of 50.2×10^6 $m.s^{-1}$ for the matrix, *i.e.* ten times larger. Such a fact has been already observed in a previous study on carbon oxidation by water vapor [55].

5. Optimization of the oxidation behavior and design of porous C/C composites

In the preceding sections, we have demonstrated how the model could be used to perform identification of previously unreachable chemical rate constants. Now, we will show how the model can be operated in other ways. First, we will evalu-

ate the sensitivity of the oxidation behavior with respect to material parameters; second, we will use the model as a prediction and designing tool.

5.1. Sensitivity of the identified parameters to the model input data

The aim of this section is to sense the influence of the parameters on different morphological and kinetic variables. For every one of them, several equations from Section 3 had to be recombined in order to limit mutual dependences between parameters themselves. A variation of ± 10% is applied on each parameter, maintaining the other ones fixed. Fig. 11 illustrates the dependencies.

5.1.1. Post-test morphological features

Eqs. 16 and 22 and the simplified expression of $\mathcal{A}$ are used to assess the influence of the parameters for the overall affected length δ_a on Fig. 11a. An increase in either fibers or matrix volume fractions (*i.e.* a decrease of porosity) decreases δ_a. For the matrix volume fraction solely, this has been experimentally demonstrated in Sections 2.2 and 4.2.2, as the matrix behaves as a protection for the fibers. Conversely, when it decreases, the exposed surface is increased, which enhances the overall reaction. One can notice that the matrix charateristic length $d_m^\star$ does not influence too much δ_a. On the other hand, it is largely dominated by $d_f^\star$, suggesting that the mean pore size of the fibrous architecture impacts the material behavior at the first order. Indeed, δ_a follows quite logically the evolutions of $d_f^\star$ and of the diffusion capacity: the less porous the material is and the lower the diffusion coefficient is, the less it is affected indepth. The geometrical diffusion parameters also seem to be impact factors: an increase in η_{lim} and in γ strongly decreases δ_a. The heterogeneous reactivity of the fibers plays a much larger role in the establishment of δ_a than the matrix one. This is logical considering that the amount and the manner in which the oxidizing species are diffusing in-depth depend on the way that they are consumed at first by the fibers.

From Eq. 23a and the expression of $\mathcal{A}$, parameters dependence for ξ_i is determined. An increase in the matrix volume fraction was experimentally proven to decrease the affected length δ_a, but it apparently also decreases ξ_i according to Fig. 11b. This means that δ_f decreases faster that δ_a when $\phi_{m,0}$ is increased and the fibers are more protected by the matrix. A similar trend is observed for the fibers heterogeneous reactivity. This highlights the fact that the more reactive the fibers are, the less they will be stripped of the matrix and the oxidation reaction will be maintained at the surface of the material. On the other hand, Fig. 11a indicates that an increase of 10% in the matrix heterogeneous reactivity decreases δ_a by less than 1%. However, the same increase in $k_{het,m}$ will increase ξ_i by more than 3%, meaning that increasing the matrix heterogeneous reactivity impacts the denudation of the fibers more than the overall affected length.

5.1.1.1 Heterogeneous kinetics

Eqs. 19a, 19b, 23a and the expression of $\mathcal{A}$ are combined to assess $k_{het,f}$ and $k_{het,m}$ parameters dependencies. Fig. 11c illustrates that δ_a plays a major role in the identification of $k_{het,f}$ in accordance with what is mentioned above. However, it plays a much larger role in the evolution of $k_{het,m}$, especially when it is underestimated, as displayed on Fig. 11d. Logically, the fibers affected length δ_f also has a strong impact on $k_{het,m}$. Besides, one can notice that globally the architectural parameters have a greater impact on the value of $k_{het,f}$ and $k_{het,m}$ than on δ_a and ξ_i, even if they remain parameters of lesser importance.

5.1.2. Recession rate and material effective reactivity

To assess parameters influence on the recession rate, Eqs. 22, 23a and 24 are combined and Fig. 11e illustrates the evolution. As mentioned in section 4.2.4, v_r depends at first order on the boundary concentration C_b. v_r is also influenced by parameters related to the fibers such as the fibers molar volume, their characteristic length and their heterogeneous reactivity, but is surprisingly slightly affected by matrix heterogeneous reactivity and fibers and matrix volume frac-

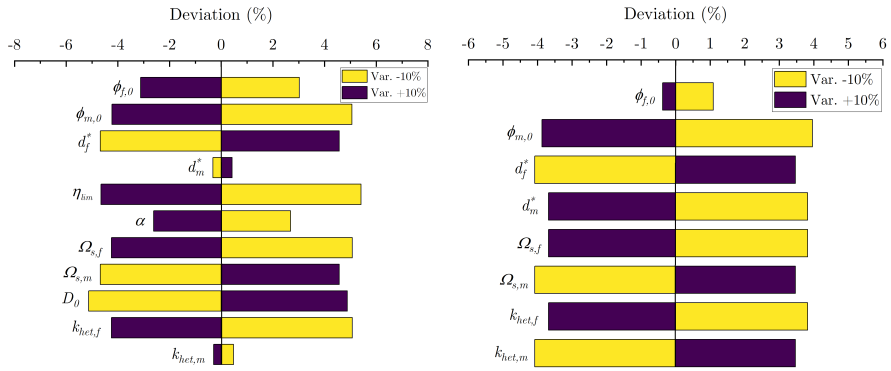

(a) Overall affected depth δ_a

(b) Affected lengths ratio ξ_i

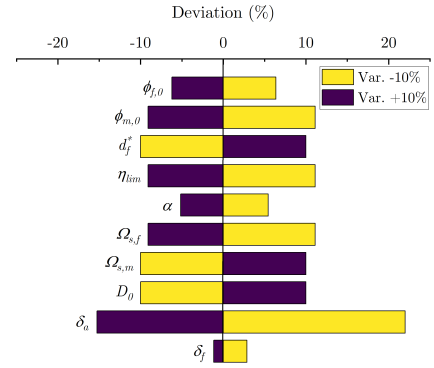

(c) Fiber reactivity $k_{het,f}$

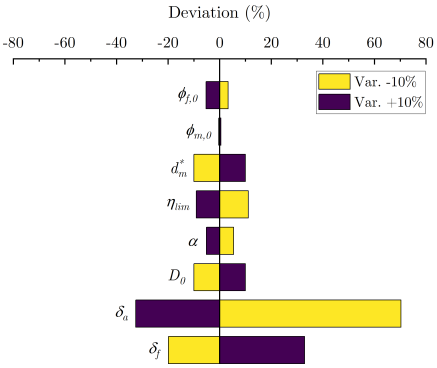

(d) Matrix reactivity $k_{het,m}$

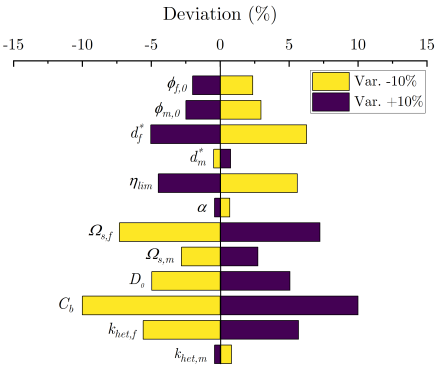

(e) Composite recession rate v_r

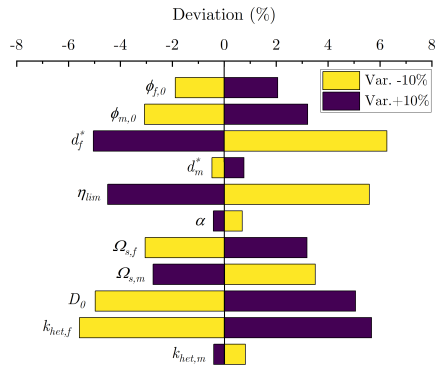

(f) Composite effective reactivity k_{eff}

Figure 11: Parameters influence on after test morphological features, fibers and matrix heterogeneous kinetics, recession rate and material effective reactivity. **color should be used for that figure.**

tions. Besides, v_r varies logically with fibers and matrix volume fractions as observed in the experimental section. Fig. 11e also displays an interesting trend: the material's recession rate decreases when the geometrical diffusion parameters of the fibrous architecture increase.

The influence on the material effective reactivity is inferred from the relation $k_{\text{eff}} = \dfrac{v_r}{v_c}$. Thus, k_{eff} is not influenced any more by the boundary concentration and depends only modestly on the fibers molar volume and fibers and matrix volume fractions. However, its evolution with fibers and matrix volume fraction is completely in contrast with the recession rate's. The effective reactivity is also greatly enhanced by the fibers heterogeneous reactivity. As demonstrated for δ_a in Section 5.1.1, this suggests that the material behavior is dominated by the fibers. Similarly to the recession rate, the geometrical diffusion parameters seem to reduce the effective reactivity of the material, as they impede internal gas transport. This analysis is supported by the fact that the diffusion coefficient is also a parameter of influence for k_{eff} that tends to decrease it.

In conclusion, the observed trends are consistent with the experimental observations. One can notice that architectural parameters do not influence to a larger extent the post-test morphologies, the recession rate and the effective reactivity when they are considered individually, but a simultaneous variation of all of them can have a greater impact. To conclude, graphs from Fig. 11 allow one to visually assess the impact of the different parameters and this provides guidelines in a material conception process. This will be explored in more detail in the forthcoming section.

5.2. Analytical modeling as a prediction and designing tool

In this part, the trends obtained in Section 3 will be intepreted and discussed in order to extensively exploit the model. First, a few equations will be reassorted to split the contributions of the architectural parameters from those of reaction kinetics in the material response.

5.2.1. Evolutions of the affected length

Eqs. 22 and 23a are rearranged into the following expression:

$$\lambda_m^2 Sh_m = \frac{\Sigma_m}{\Phi_0(1-\xi_i)} \tag{27}$$

with $(1-\xi_i)$ being a function of $\mathcal{F}$, itself a function of kinetic and structural parameters. As a consequence, for a specified value of $\mathcal{F}$, Eq. 27 indicates that $\dfrac{\delta_a}{d_m^\star}$, which is the extent of volumic oxidation compared to the matrix characteristic length, depends in a rather straightforward way on the matrix Sherwood number and on a combination of kinetic contrast and architectural parameters. The following two limiting cases are identified:

$$\begin{cases} \lim\limits_{\mathcal{F}\to 0} \lambda_m^2 Sh_m = \dfrac{1}{\Phi_0}\left(\Sigma_m + \dfrac{9}{8}\mathcal{F}\right) & \text{(28a)} \\ \lim\limits_{\mathcal{F}\to \infty} \lambda_m^2 Sh_m = \dfrac{3\mathcal{F}}{\Phi_0} & \text{(28b)} \end{cases}$$

Fig. 12 illustrates the evolution of $\lambda_m^2 Sh_m$ in three different kinetic situations according to $\mathcal{F}$. For any value of $\mathcal{F}$, $\dfrac{\delta_a^2}{d_m^{\star 2}}$ decreases with increasing values of $\phi_{m,0}$, or $\phi_{f,0}$, or both, which suggests the overall affected length might be reduced by decreasing porosity. However, as δ_a will never equal 0, a non-negligible remaining affected length has to be considered, even for very dense materials. Furthermore, as mentioned above from the analysis of Fig. 7, ξ_i decreases with the matrix volume fraction for a fixed fibers volume fraction. This means that the fibers affected length δ_f also decreases with matrix volume fraction. The same conclusion was made throughout the parameters sensitivity analysis in Section 5.1.1.

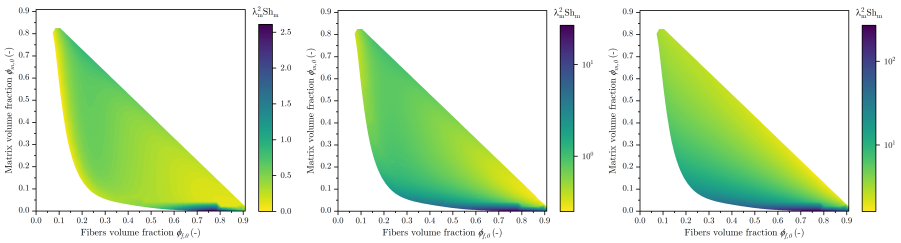

(a) $\mathcal{F} \ll 0.1$ (b) $\mathcal{F} = 0.1$ (c) $\mathcal{F} \gg 0.1$

Figure 12: Graphs corresponding to Eq. 27 for three values of $\mathcal{F}$ in the $\left\{\phi_{f,0}; \phi_{m,0}\right\}$ parameter space. **color should be used for that figure.**

One can notice on Fig. 12 that minimum values of $\dfrac{\delta_a^2}{d_m^{\star 2}}$ would always be obtained for non-porous composites with the highest fibers volume fractions for any value of $\mathcal{F}$.

A comparison between Figs. 12a and 12c suggests that the dimensionless affected length is much less sensitive to the fibers volume fraction when $\mathcal{F}$ is large, *i.e.* when the matrix is much more reactive than the fibers.

Similar results can be obtained taking the fibers instead of the matrix as reference. By rearranging Eqs. 19a and 19b, we obtain (see Appendix D.3 for details):

$$\lambda_f^2 Sh_f = \frac{9}{2}\frac{\upsilon_m}{\upsilon_f}\frac{1}{\xi_i\left(4-\frac{5}{2}\xi_i\right)}\Phi_0^{-1} \tag{29}$$

where ξ_i is still a function of $\mathcal{F}$. As before, two limiting regimes are identified:

$$\begin{cases} \lim\limits_{\mathcal{F}\to 0} \lambda_f^2 Sh_f = \dfrac{\upsilon_m}{\upsilon_f}\dfrac{1}{\Phi_0}\left(\dfrac{\Sigma_m}{\mathcal{F}}+\dfrac{9}{8}\right) & \text{(30a)} \\ \lim\limits_{\mathcal{F}\to \infty} \lambda_f^2 Sh_f = 3\dfrac{\upsilon_m}{\upsilon_f}\dfrac{1}{\Phi_0} & \text{(30b)} \end{cases}$$

An illustration of the evolution of $\lambda_f^2 Sh_f$, for three specific kinetics cases with respect to the fibers and matrix fractions, is given in Appendix F.1.

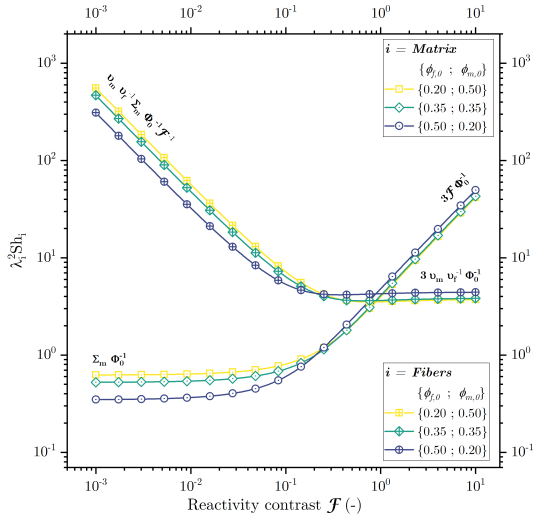

Figure 13: Graphs corresponding to Eqs. 27 and 29 for three fixed combinations of $\{\phi_{f,0};\phi_{m,0}\}$. **color should be used for that figure.**

Fig. 13 sums up the evolution of $\lambda_i^2 Sh_i$ ($i \in \{f;m\}$) with $\mathcal{F}$ for three combinations of $\{\phi_{f,0};\phi_{m,0}\}$ at a fixed total solid volume fraction equal to 0.7. When $\mathcal{F}$ is low (*resp.* high), $\lambda_f^2 Sh_f$ (*resp.* $\lambda_m^2 Sh_m$) strongly varies, meaning that the kinetic behavior of the system is logically controlled by the fibers (*resp.* matrix) with a slope of $-\dfrac{\upsilon_m}{\upsilon_f}\dfrac{\Sigma_m}{\Phi_0}$ (*resp.* $\dfrac{3}{\Phi_0}$) given by Eq. 30a (*resp.* 28b). Whereas, in the other domain, $\lambda_f^2 Sh_f$ and $\lambda_m^2 Sh_m$ remain constant with a value of $3\dfrac{\upsilon_m}{\upsilon_f}\Phi_0^{-1}$ and $\Sigma_m \Phi_0^{-1}$ respectively given by Eqs. 30b and 28a. According to Fig. 13, with the chosen combination of solid volume fractions, it appears that the material behavior is less controlled by architectural parameters in the domain kinetically controlled by the matrix as $\lambda_i^2 Sh_i$ can be strongly reduced when the fibers (*resp.* matrix) rate increases (*resp.* decreases) for low values of $\mathcal{F}$, but slightly increases for high values of $\mathcal{F}$. Furthermore, the value of $\mathcal{F}$ for which the transition of the material behavior occurs (around $\mathcal{F} = 0.1$), decreases when fibers (*resp.* matrix) volume fraction increases (*resp.* decreases) indicating that the delimitation of the kinetically controlled domains is not only dependent on the reactivity constrast, but also on architectural parameters.

The equations and figures provided in this section can be used to determine optimal sets of parameters $\{\phi_{f,0}; \phi_{m,0}\}$ that will minimize the overall affected length δ_a in specific physicochemical conditions.

650

5.2.2. Effective reactivity

The same method will be applied to assess material effective reactivity. Defining a Sherwood number for the composite as $Sh_c = \dfrac{k_{\text{eff}}\eta_{lim}d_m^\star}{D_0}$, the combination of Eqs. 25 and 27 satisfies:

$$\frac{Sh_c}{\sqrt{Sh_m}} = 2\sqrt{\frac{\Phi_0}{\Sigma_m}}\frac{\sqrt{(1-\xi_i)}}{\xi_i + \frac{\Phi_0}{3}\frac{\upsilon_c}{\upsilon_m}(4-\xi_i)} \tag{31}$$

As before, two limiting regimes are defined:

$$\begin{cases} \lim\limits_{\mathcal{F}\to 0}\dfrac{Sh_c}{\sqrt{Sh_m}} = \dfrac{3}{2}\sqrt{\dfrac{1}{\Sigma_m\Phi_0}}\dfrac{\upsilon_m}{\upsilon_c} & \text{(32a)} \\ \lim\limits_{\mathcal{F}\to \infty}\dfrac{Sh_c}{\sqrt{Sh_m}} = \dfrac{2\sqrt{\Phi_0\Sigma_m}}{1+\frac{\upsilon_c}{\upsilon_m}\Phi_0}\mathcal{F}^{-1} & \text{(32b)} \end{cases}$$

Fig. 14 illustrates Eq. 31 in three different kinetics states according to $\mathcal{F}$. For low values of $\mathcal{F}$, Sh_c can be much higher than the matrix rate Sh_m, especially when $\phi_{m,0}$ is low and $\phi_{f,0}$ is high. This means that the composite kinetics
655 strongly depends on the fibers behavior and it decreases drastically when a few matrix is added. When $\mathcal{F}$ increases, the dependency of $\frac{Sh_c}{\sqrt{Sh_m}}$ on $\phi_{m,0}$ goes from decreasing to increasing. Besides, for increasing values of $\mathcal{F}$, the composite effective reactivity remains lower than that of the matrix and the highest values for $\frac{Sh_c}{\sqrt{Sh_m}}$ are now determined for moderate fiber volume fractions and
660 very low porosity values. The decline of $\dfrac{Sh_c}{\sqrt{Sh_m}}$ from Fig. 14a to 14c indicates that when the matrix is the most reactive phase, its weight in the kinetics balance is diluted because of the protective effect of the fibers that are less reactive.

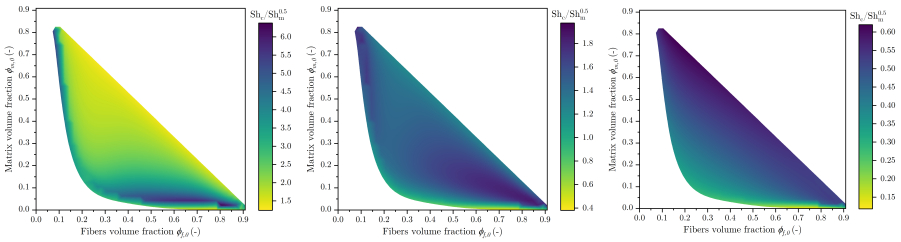

(a) $\mathcal{F} \ll 0.1$ (b) $\mathcal{F} = 0.1$ (c) $\mathcal{F} \gg 0.1$

Figure 14: Graphs corresponding to Eq. 31 for three values of $\mathcal{F}$ in the $\{\phi_{f,0}; \phi_{m,0}\}$ parameter space. **color should be used for that figure.**

The effective reactivity of the composite can also be defined by $Sh_c = \dfrac{k_{\text{eff}} \eta_{lim} d_f^\star}{D_0}$ and Eq. 31 can be reassorted combining the fibers Sherwood number, the expression of $\mathcal{A}$ and the ratio of fibers and matrix characteristic lengths:

$$\frac{Sh_c}{\sqrt{Sh_f}} = 2\sqrt{\frac{A\Phi_0}{\Sigma_m}}\sqrt{\frac{d_f^\star}{d_m^\star}}\sqrt{\frac{\upsilon_f}{\upsilon_m}}\frac{\sqrt{(1-\xi_i)}}{\xi_i + \frac{\Phi_0}{3}\frac{\upsilon_c}{\upsilon_m}(4-\xi_i)} \tag{33}$$

The following limiting regimes are defined:

$$\begin{cases} \lim\limits_{\mathcal{F}\to 0} \dfrac{Sh_c}{\sqrt{Sh_f}} = \dfrac{9}{2\sqrt{2}}\sqrt{\dfrac{d_f^\star}{d_m^\star}}\dfrac{\sqrt{\Omega_{s,f}\Omega_{s,m}}}{\Omega_{s,c}}\dfrac{\sqrt{\mathcal{F}}}{\sqrt{\Phi_0}\Sigma_m} & \text{(34a)} \\ \lim\limits_{\mathcal{F}\to \infty} \dfrac{Sh_c}{\sqrt{Sh_f}} = \sqrt{2}\sqrt{\dfrac{d_f^\star}{d_m^\star}}\sqrt{\dfrac{\upsilon_f}{\upsilon_m}}\dfrac{\sqrt{\Phi_0}}{\Phi_0\frac{\upsilon_c}{\upsilon_m}+1}\mathcal{F}^{-\frac{1}{2}} & \text{(34b)} \end{cases}$$

An illustration of the evolution of $\frac{Sh_c}{\sqrt{Sh_f}}$, for three specific kinetics cases with respect to the fibers and matrix fractions, is given in Appendix F.2.

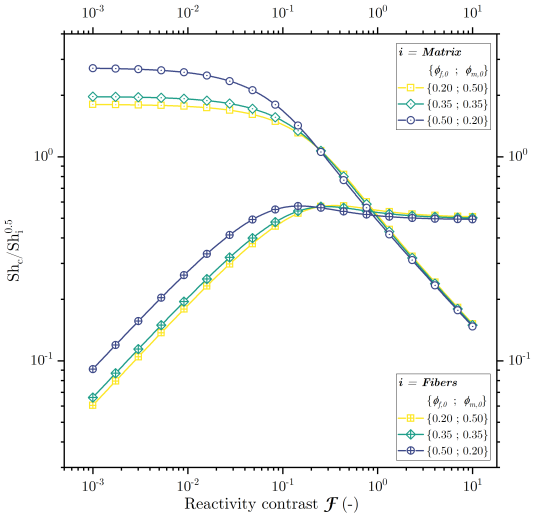

Figure 15: Graphs corresponding to Eqs. 31 and 33 for three fixed combinations of $\{\phi_{f,0};\phi_{m,0}\}$. **color should be used for that figure.**

Fig. 15 sums up the evolution of $\dfrac{Sh_c}{\sqrt{Sh_i}}$ $(i \in \{f;m\})$ with $\mathcal{F}$ for three fixed combinations of $\{\phi_{f,0};\phi_{m,0}\}$. As mentioned above for the evolution of $\lambda_i^2 Sh_i$, $\dfrac{Sh_c}{\sqrt{Sh_i}}$ varies strongly in the domain where the concerned phase is dominating and remains constant in the other domain.

5.2.3. Optimization of the resistance to oxidation

Fig. 13 reveals that the reduction of the affected length by oxidation is ideal when fibers and matrix have close reactivities (meaning $\mathcal{F}$ close to 0.1), as the curves of $\lambda_f^2 Sh_f$ and $\lambda_m^2 Sh_m$ vary symetrically with the slopes previously identified by Eqs. 30a and 28b around the transition value of $\mathcal{F}$.

Similarly, one can notice on Fig. 15 that $\dfrac{Sh_c}{\sqrt{Sh_f}}$ and $\dfrac{Sh_c}{\sqrt{Sh_m}}$ both increases symmetrically around the transition $\mathcal{F}$. This means that when the fibers and the matrix display almost the same reactivity, the composite effective reactivity is maximized for the chosen combination of solid volume fractions. It does not represent an optimal situation, conversely to what has been concluded concerning the affected depth.

In order to assess to which extent the material efficiency is dependent on external conditions, let us select from Figs. 12 and 14 the combinations of solid volume fractions $\{\phi_{f,0};\phi_{m,0}\}$ which minimize $\lambda_m^2 Sh_m$ and $\dfrac{Sh_c}{\sqrt{Sh_m}}$ separately in the two extreme kinetic domains. The corresponding curves are given on Fig. 16.

For $\mathcal{F} < 0.1$ and $\mathcal{F} > 0.1$, the solid volume fractions combination that reduces the affected length does not yield to the lowest value of $\dfrac{Sh_c}{\sqrt{Sh_m}}$, but instead increases it by a factor of up to 4. On the other hand, if one picks the $\{\phi_{f,0};\phi_{m,0}\}$ combination minimizing the effective reactivity, $\lambda_m^2 Sh_m$ is larger by a factor of up to 12 compared to its lowest potential value. Besides, discrepancies are higher in the domain controlled by the matrix (*i.e.* $\mathcal{F} > 0.1$).

To conclude on the optimization of the resistance to oxidation, Fig. 16 indicates that the affected length and the effective reactivity cannot be minimized at the same time. As Sh_m does not vary when $\mathcal{F}$ is fixed, the affected length equals up to 3.5 times its lowest potential value when the effective reactivity is minimized; and 4 times for Sh_c in the converse case, for every value of $\mathcal{F}$. Then, the loss of optimization seems equivalent between the affected length and the effective reactivity. Finally, none of the kinetic situations $\mathcal{F} < 0.1$ or $\mathcal{F} > 0.1$ is more advisable than the other. The same conclusions would be given with respect to the fibers.

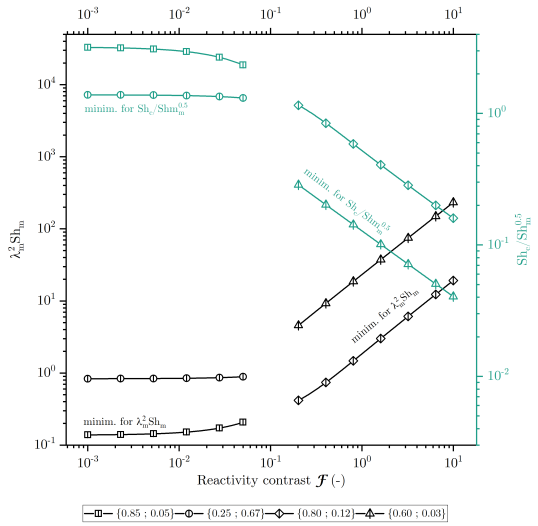

Figure 16: Graphs corresponding to Eqs. 27 and 31 with $\mathcal{F}$ for specific combinations of $\{\phi_{f,0}; \phi_{m,0}\}$ (minim. = minimization). **color should be used for that figure.**

In practice, one has to face a binary choice. On the one hand, decreasing Sh_c means that the effective reactivity of the composite is decreased. However, the immediate consequence is that the affected length is not optimal. In realistic conditions of use, this might increase the damage by mechanical erosion. On the other hand, one could think of diminishing δ_a, which would minimize mechanical erosion, but this leads to a non optimal effective reactivity.

It is recalled that Sh_c is a dimensionless parameter which contains v_r but also depends on C_b (which depends on the flow conditions) and v_c (which is itself a function of the fibers and matrix volume fractions). Therefore, optimizing the recession rate v_r not only depends on Sh_c, but also on these other two parameters.

6. Conclusions

In this work, a simple one-dimensional analytical model describing the behavior of porous 3D needled C/C composites under oxidation has been set up. It pro-

vides expressions for the recession rate and the lengths of the oxidation-affected zones as functions of the physicochemical conditions and of the material structural and kinetic parameters.

The model has been put in front of an experimental methodology in order to validate it and to use it for the identification of yet unknown parameters. Isothermal oxidation TGA experiments under dry air have been carried out on 3D needle-punched C/C composites featuring variable matrix volume fractions at temperatures between 1173K and 1373K. Even though oxidation conditions and porous C/C of variable matrix fractions are not representative of a real nozzle throat environment, they have been aptly choosen in order to provide simple and appropriate configurations in order to validate the modeling and identification methodology. Thus, oxidation rates and morphological evolutions were collected. CFD computations have been used to retrieve the boundary concentrations and the apparent effective rates of the different materials surfaces. An innovative characterization method combining X-ray µCT and 3D-image correlation, with good accuracy and confidence in the results, was used to determine the fibers and matrix affected lengths. Based on these data and on the experimental recession rates, the increasing robustness of C/C composites to oxidation with matrix volume fraction has been proven.

Fibers and matrix heterogeneous kinetic rate constants have been identified. Activation energies of 192.4 and 202.2 $kJ.mol^{-1}$ were determined for the fibers and the matrix respectively. They were found out to be consistent with the post-test morphological observations and with a literature survey. For the first time, the identification of an Arrhenius law for the oxidation of a Rough Laminar pyrocarbon matrix at high temperatures in dry air has been made. This particular result is a novel contribution to the study of pyrocarbons in general. The influence of the material parameters on the oxidation behavior has been assessed through the obtained equations and confirmed by the experimental results. Several major observations might be upheld. C/C composites oxidation robustness (*i.e.* short affected lengths by oxidation and low recession rates) increases with respect to the matrix solid fraction, in accordance with the ex-

perimental behavior. The post-test morphological aspect of the material (*i.e.* δ_a) is greatly impacted by the characteristic length (*i.e.* initial pore size) of the fibrous preform and by the heterogeneous reactivity of the fibers, more than by the matrix ones. On the other hand, the geometrical diffusion parameters tend to have a positive effect on the oxidation robustness of the material by decreasing simultaneously its recession rate, its effective reactivity and the overall affected length by oxidation. In addition, when the matrix is more reactive than the fibers, its negative impact on the composite effective reactivity is mitigated by the presence of the fibers. Finally, architectural parameters taken individually do not impact significantly the affected lengths and the recession rate, but that cumulated variations on everyone of them might have a susbtantial effect. Another significant result of this study is the impossibility of minimizing simultaneously the overall affected length of the material and its effective reactivity with respect to the matrix volume fraction. Compromises have to be made considering the final application of the material, such as the presence of mechanical erosion.

Further improvements could be brought to this model in a more elaborated version. The porosity distribution (based on the pores diameter distribution) instead of a global porosity could be considered for more accuracy. On the other hand, the validation of the model is mainly based on the variation of the volume fraction of the matrix, which provides satisfaction for the targeted nozzle throat application, but its accuracy might also be verified while making the volume fraction of the fibers vary. The main limitation of this methodology relies on the limited robustness of the CFD simulations to compute the recession rate. Additional improvements are considered to provide more accuracy in the identification of the boundary conditions. Further work is also envisaged on confronting this model to an image-based three-dimensional numerical approach as performed by Vignoles *et al.* [20] in order to bring another order of validation. Identifying the fibers and the matrix heterogeneous kinetics in CO_2 and H_2O-containing environments, by means of the above-developed

analytical model, is considered. This approach could be validated using the data experimentally identified in the work of Fradin *et al.* [52]. Also, repeating the same experimental protocol on C/C composites containing other types of low-temperature pyrocarbons (Smooth Laminar, Dark Laminar, Regenerative Laminar, Isotropic) would bring a new perspective on the structure-reactivity relationship in this family of materials.

Appendices

A. In-house DVC code

The registration is performed using an in-house digital volume correlation software. The sought mapping is assumed to be described by a global affine transformation, including rigid translation and rotation of the specimen. It also possibly includes an isotropic scaling to accommodate small variations in the images resolution. Also, prior to the registration, images are standardized to mitigate differences in brightness and contrast between specimens. The transformation parameters are found by minimizing the gray level residual between the mapped image and the reference one.

B. Pores diameter distribution

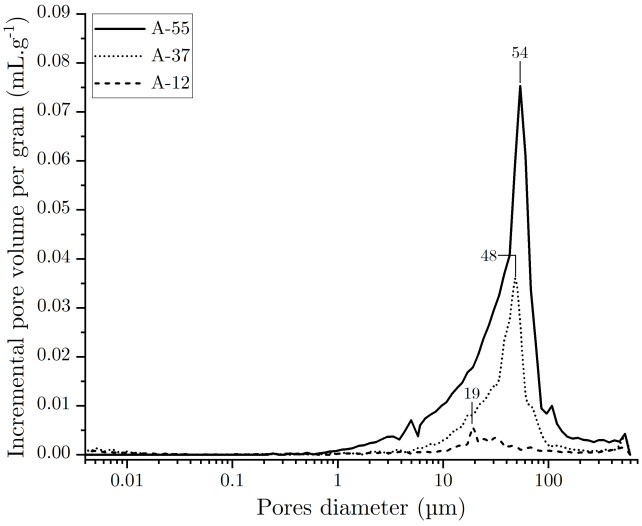

Figure B.1: Pores diameter distribution of the three types of densified C/C.

A Micromeritics Autopore IV 9510 mercury porosimeter, with two pressure ports (high and low pressures), is employed to characterize the pores size distribution before and after test. A contact angle of 130° is chosen to compute the

Washburn law. The full size range of the scanned pores is between 0.004 µm and 600 µm.

C. Experimental mass loss rate evolution

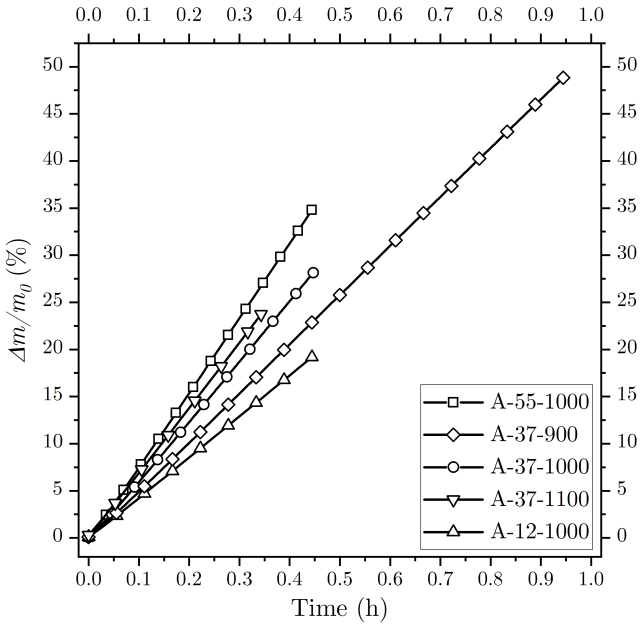

Figure C.1: Evolution with time of the mass loss rate under oxidation compared to the initial mass.

D. Analytical problem solution details

D.1. Solutions for the solids and gas mass balances

Following the consideration of a steady state regime within a moving reference frame with velocity v_r, we perform a coordinate change $x' = x - v_r t$; $t' = t$.

Eqs. 12a, 12b and 13 from the main manuscript are transformed as follows:

$$\begin{cases} v_r \dfrac{d\phi_f}{dx'} = \Omega_{s,f}\sigma_{v,f}(\phi_f)k_{het,f}C & \text{(D.1a)} \\ v_r \dfrac{d\phi_m}{dx'} = \Omega_{s,m}\sigma_{v,m}(\phi_m)k_{het,m}C & \text{(D.1b)} \\ v_r \dfrac{dC}{dx'} + \dfrac{d}{dx'}\left((1-\phi_m-\phi_f)^\gamma \dfrac{D_0}{\eta_{lim}}\dfrac{dC}{dx'}\right) - v_r\Omega_{s,m}^{-1}\dfrac{d\phi_m}{dx'} - v_r\Omega_{s,f}^{-1}\dfrac{d\phi_f}{dx'} = 0 & \text{(D.1c)} \end{cases}$$

A prime integral appears:

$$C + (1-\phi_m-\phi_f)^\gamma \frac{D_0}{\eta_{lim}v_r}\frac{dC}{dx'} - \phi_m\Omega_{s,m}^{-1} - \phi_f\Omega_{s,f}^{-1} = I_1 \qquad \text{(D.2)}$$

Looking at the boundary $x' \to \infty$ where the gas is completely depleted, it is recognized that I_1 is equal to $-\phi_{m,0}{\Omega_{s,m}}^{-1} - \phi_{f,0}{\Omega_{s,f}}^{-1}$. Thus, Eq. D.2 now becomes:

$$C + (1-\phi_m-\phi_f)^\gamma \frac{D_0}{\eta_{lim}v_r}\frac{dC}{dx'} - (\phi_m-\phi_{m,0})\,\Omega_{s,m}^{-1} - (\phi_f-\phi_{f,0})\,\Omega_{s,f}^{-1} = 0 \qquad \text{(D.3)}$$

For convenience, the following dimensionless quantities are introduced:

$$\begin{cases} \chi = \dfrac{C}{C_b} & \text{(D.4a)} \\ \xi = \dfrac{x'}{\delta_a} & \text{(D.4b)} \end{cases}$$

Eq. D.3 can be rewritten as:

$$\chi + (1-\phi_m-\phi_f)^\gamma P^{-1}\frac{d\chi}{d\xi} - \phi_m{\upsilon_m}^{-1} - \phi_f{\upsilon_f}^{-1} + \upsilon_c^{-1} = 0 \qquad \text{(D.5)}$$

where a dimensionless number $P = \dfrac{v_r\delta_a\eta_{lim}}{D_0}$ appears. An *effective* molar volume $\Omega_{s,c}$, or *composite* molar volume, can be defined as follows:

$$\phi_{m,0}\Omega_{s,m}^{-1} + \phi_{f,0}\Omega_{s,f}^{-1} = \Omega_{s,c}^{-1} \qquad \text{(D.6)}$$

and condensation ratios, which are dimensionless parameters, are also introduced as:

$$\upsilon_i = C_b\Omega_{s,i} \;\; i \in \{f;m;c\} \qquad \text{(D.7)}$$

Eqs. D.1a and D.1b can be re-written as follows:

$$\begin{cases} \dfrac{d\phi_f}{\tilde{\sigma}_{v,f}(\phi_f)dx'} = A_f\chi_f(\xi)d\xi & \text{(D.8a)} \\ \dfrac{d\phi_m(\xi)}{\tilde{\sigma}_{v,m}(\phi_m)dx'} = A_m\chi_m(\xi)d\xi & \text{(D.8b)} \end{cases}$$

where $A_f = 4\sqrt{\phi_{f,0}}\upsilon_f Sh_f P^{-1}\lambda_f^2$ and $A_m = 4\upsilon_m Sh_m P^{-1}\lambda_m^2$. Sh_i are known as Sherwood numbers and λ_i are characteristic length ratios. These dimensionless parameters are defined by:

$$Sh_i = \frac{k_{het,i} d_i^\star \eta_{lim}}{D_0} \; i \in \{f; m\} \tag{D.9}$$

$$\lambda_i = \frac{\delta_a}{d_i^\star} \; i \in \{f; m\} \tag{D.10}$$

From Eqs. D.8a and D.8b, a relation between solid volume fraction profiles and concentration profiles may be found:

$$\int_0^\xi \chi(\xi)\, d\xi = A_f^{-1} \int_0^{\phi_f(\xi)} \tilde{\sigma}_{v,f}^{-1}(\phi_f)\, d\phi_f + A_m^{-1} \int_0^{\phi_m(\xi)} \tilde{\sigma}_{v,m}^{-1}(\phi_m)\, d\phi_m \tag{D.11}$$

A convenient approximation consists in splitting Eq. D.11 in two parts over space, introducing a normalized ordinate ξ_i indicating the position of a separation between two domains, as illustrated by Fig. 5:

$$\begin{cases} \displaystyle\int_0^\xi \chi(\xi)\, d\xi = A_f^{-1} \int_0^{\phi_f(\xi)} \tilde{\sigma}_{v,f}^{-1}(\phi_f)\, d\phi_f \text{ for } \xi \in [0; \xi_i] & \text{(D.12a)} \\ \displaystyle\int_{\xi_i}^\xi \chi(\xi)\, d\xi = A_m^{-1} \int_0^{\phi_m(\xi)} \tilde{\sigma}_{v,m}^{-1}(\phi_m)\, d\phi_m \text{ for } \xi \in [\xi_i; 1] & \text{(D.12b)} \end{cases}$$

An appropriate definition for ξ_i is:

$$\xi_i = \frac{\delta_f}{\delta_a} \tag{D.13}$$

where δ_f would be the fiber oxidation affected length as defined by Fig. 5.

In this approximation, the fiber solid volume fraction is equal to the fraction $\phi_{f,0}$ present in the pristine material as soon as $\xi \geq \xi_i$, and the matrix volume fraction goes to the pristine material value $\phi_{m,0}$ when ξ goes to 1. The solution may be approximated by picking candidate functions for $\chi(\xi)$ in the two intervals: let us call them $\chi_f(\xi)$ and $\chi_m(\xi)$, respectively. For sake of simplicity, a 2^{nd} order polynomial is chosen for the fibers-only domain (Eq. D.14a) and a 3^{rd} order polynomial for the fiber+matrix domain (Eq. D.14b). Let us define the

normalized concentration at the interface between both domains as $\chi_i = \chi(\xi_i)$. To alleviate further notations, in the fibers+matrix domain, ξ can be substituted with $\xi' = \dfrac{\xi - \xi_i}{1 - \xi_i}$.

$$\begin{cases} \chi_f(\xi) = 1 - a\dfrac{\xi}{\xi_i} - b\left(\dfrac{\xi}{\xi_i}\right)^2 & \text{(D.14a)} \\ \chi_m(\xi) = \chi_i\left(1 - \dfrac{3}{2}\xi' + \dfrac{1}{2}\xi'^3\right) & \text{(D.14b)} \end{cases}$$

where the polynomial coefficients a and b are determined assuming that the concentration and its first derivative are continous at the interface i:

$$\begin{cases} \chi_f(\xi_i^-) = \chi_m(\xi_i^+) & \text{(D.15a)} \\ \chi'_f(\xi_i^-) = \chi'_m(\xi_i^+) & \text{(D.15b)} \end{cases}$$

a and b are found to be equal to:

$$a = \frac{1}{3}\upsilon_m^{-1} P\Phi_0(\xi_i - 4) + 2 \tag{D.16}$$

$$b = \frac{1}{3}\upsilon_m^{-1} P\Phi_0(\xi_i + 2) - 1 \tag{D.17}$$

using the dimensionless structural parameter Φ_0.

From the same assumptions, an expression for χ_i may be found:

$$\chi_i = \frac{2}{3}\frac{\Phi_0 P}{\upsilon_m}(1 - \xi_i) \tag{D.18}$$

By taking up the conditions that $\phi_f(\xi = \xi_i) = \phi_{f,0}$ and $\phi_m(\xi' = 1) = \phi_{m,0}$, one may obtain:

$$\begin{cases} A_f = \dfrac{18\sqrt{\phi_{f,0}}\upsilon_m}{\Phi_0 P\xi_i\left(4 - \frac{5}{2}\xi_i\right)} & \text{(D.19a)} \\ A_m = \dfrac{4\Sigma_m\upsilon_m}{\Phi_0 P(1 - \xi_i)} & \text{(D.19b)} \end{cases}$$

where Σ_m is the integral of $\tilde{\sigma}_{v,m}^{-1}(\phi_m)$ from ξ_i to 1. For an easy calculation, a polynomial approximation has been taken for $\tilde{\sigma}_{v,m}^{-1}(\phi_m)$ prior to integration. As

a result, $\Sigma_m(\varepsilon)$ is approximated by:

$$\Sigma_m = \mathcal{P}(\varepsilon_{f,0}) - \mathcal{P}(\varepsilon_0) \tag{D.20}$$

where $\mathcal{P}(\varepsilon) = I'\varepsilon + J'\varepsilon^2 + K'\varepsilon^3 + L'\varepsilon^4 + M'\varepsilon^5 + N'\varepsilon^6$, ε_0 equals $1 - \phi_{f,0} - \phi_{m,0}$ and $\varepsilon_{f,0}$ accounts for $1 - \phi_{f,0}$. Polynomial parameters are listed in Table .

Coefficient	**Values**
I'	11.8
J'	-65.7
K'	211.5
L'	-374.6
M'	344.5
N'	-127.7

Table : Parameters for $\mathcal{P}(\varepsilon)$ in Eq. D.20.

Fig. D.1 illustrates the evolution of Σ_m with the architectural parameters $\phi_{f,0}$ and $\phi_{m,0}$. Due to the methodology used by Charles *et al.* [44], Σ_m is defined only for $\phi_{f,0} + \phi_{m,0} < 0.93$ (the percolation porosity ε_p is equal to 0.07). It is also not clearly defined for too low or too high values of $\phi_{f,0}$ and $\phi_{m,0}$ that would represent unrealistic materials.

Using the same approach, Eq. D.5 could be evaluated in each domain. Concentration profiles χ_f and χ_m are substituted back by their expressions (Eqs. D.14a and D.14b), and the resulting equations were evaluated at $\xi = 0$ for fibers and at $\xi' = 0$ for matrix respectively. χ_i is replaced by its expression from Eq.

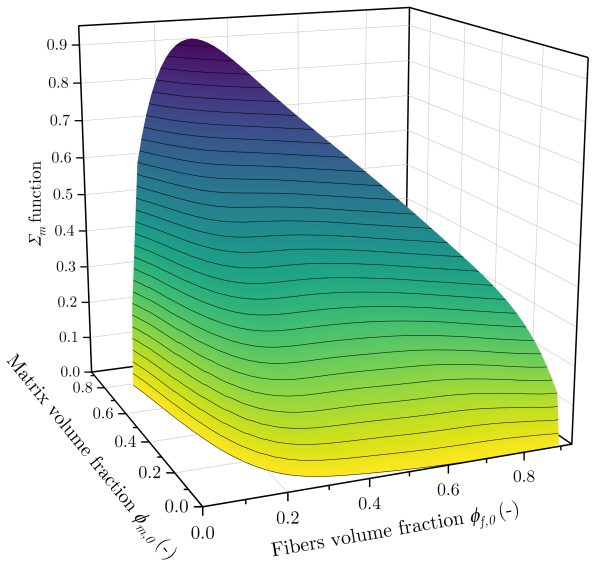

Figure D.1: Evolution of Σ_m as a function of $\phi_{f,0}$ and $\phi_{m,0}$.

D.18, yielding:

$$\begin{cases} 1 - \left(\frac{1}{3}\upsilon_m^{-1} P\Phi_0(\xi_i - 4) + 2\right) P^{-1}\xi_i^{-1} + \upsilon_c^{-1} = 0 & \text{(D.21a)} \\ \frac{2}{3}\frac{\Phi_0 P}{\upsilon_m}(1-\xi_i)\left(1 - \frac{3}{2P}\frac{(1-\phi_{f,0})^\gamma}{1-\xi_i}\right) + \phi_{m,0}{\upsilon_m}^{-1} = 0 & \text{(D.21b)} \end{cases}$$

Eqs. D.21a and D.21b provide solutions for ξ_i and P. From that point, every parameter can be determined.

Actual numerical coefficients, for example $\frac{3}{2}$ in Eq. D.21b, depend on the choice made for the concentration profile $\chi(\xi)$: they might differ for a distinct analytical model in which a different functional had been chosen for it [20]; however, they are not expected to change their order of magnitude.

D.2. Details for the identification of the heterogeneous kinetics equations and the reactivity contrast

The expression for $k_{het,f}$ is straightforwardly determined from Eq. D.19a. Knowing that χ_i satisfies Eq. D.18, an expression for $k_{het,m}$ is obtained from

Eq. D.19b:

$$\begin{cases} k_{het,f} = \dfrac{9}{2}\dfrac{D_0}{\Phi_0\eta_{lim}}\dfrac{d_f^\star}{\delta_a^2}\dfrac{1}{\xi_i(4-\frac{5}{2}\xi_i)}\dfrac{\Omega_{s,m}}{\Omega_{s,f}} & \text{(D.22a)} \\ k_{het,m} = \dfrac{D_0\Sigma_m}{\Phi_0\eta_{lim}}\dfrac{d_m^\star}{\delta_a^2}\dfrac{1}{(1-\xi_i)} & \text{(D.22b)} \end{cases}$$

The combination of Eq. D.19a and the $1-\xi_i = \Theta_m^{-2}$ relation provides a expression for the reactivity contrast as $\mathcal{A} = \dfrac{k_{het,m}}{k_{het,f}}\dfrac{\Omega_{s,m}}{\Omega_{s,f}}$:

$$\mathcal{A} = \frac{2}{9}\frac{d_m^\star}{d_f^\star}\Sigma_m \underbrace{\frac{\xi_i(4-\frac{5}{2}\xi_i)}{(1-\xi_i)}}_{\Xi(\xi_i)} \tag{D.23}$$

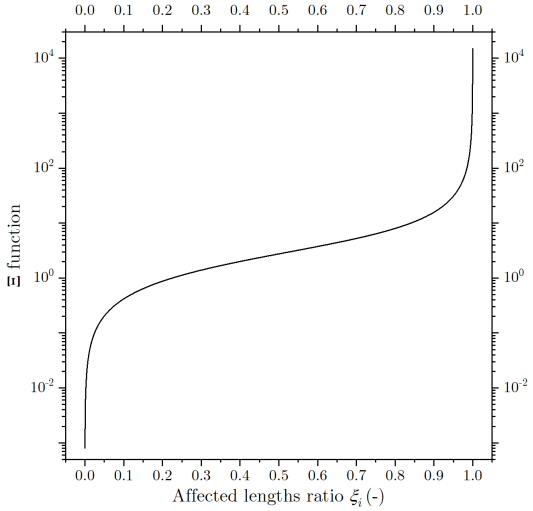

Figure D.2: Evolution of the Ξ function with ξ_i.

Fig. D.2 is a graph of Ξ (from Eq. D.23) showing the monotonous increasing, though strongly non-linear, evolution of $\mathcal{A}$ with ξ_i.

D.3. Details for the prediction of post-test morphologies

Eqs. 19a and 19b can be rearranged to make δ_a appear explicitly. However, such an expression would depend on the experimentally determined parameter

ξ_i. We must also solve the problem for ξ_i. This is done as follows.

From Eqs. 19a and 20 let us define the following set of equations:

$$\begin{cases} \dfrac{V}{\delta_a^2} = \dfrac{9}{2}\Theta_f^{-2}\dfrac{\Omega_{s,m}}{\Omega_{s,f}} & \text{(D.24a)} \\ \dfrac{U}{\delta_a^2} = \Theta_m^{-2} & \text{(D.24b)} \\ \dfrac{1}{\delta_a^2} = \dfrac{1}{5U}\left(1 - \dfrac{V}{U} + \sqrt{16 - 2\dfrac{V}{U} + \dfrac{V^2}{U^2}}\right) & \text{(D.24c)} \end{cases}$$

where $\xi_i(4 - \frac{5}{2}\xi_i) = \frac{V}{\delta_a^2}$, $\xi_i = 1 - \frac{U}{\delta_a^2}$ and $\left(1 - \frac{U}{\delta_a^2}\right)\left(3 + 5\frac{U}{\delta_a^2}\right) = 2\frac{V}{\delta_a^2}$.

An explicit expression for δ_a independent from ξ_i is inferred from the combination of Eqs. D.24a, D.24b and D.24c:

$$\frac{1}{\delta_a^2} = \frac{\Phi_0 Sh_m}{5\Sigma_m d_m^{\star 2}}\left(1 - \frac{9}{2}\frac{\mathcal{A}}{\Sigma_m}\frac{d_f^\star}{d_m^\star} + \sqrt{16 - 9\frac{\mathcal{A}}{\Sigma_m}\frac{d_f^\star}{d_m^\star} + \frac{81}{4}\frac{\mathcal{A}^2}{\Sigma_m^2}\frac{d_f^{\star 2}}{d_m^{\star 2}}}\right) \tag{D.25}$$

Eqs. D.24a and D.24b are combined to define W as:

$$W = \frac{V}{U} = \frac{9}{2}\frac{\mathcal{A}}{\Sigma_m}\frac{d_f^\star}{d_m^\star} \tag{D.26}$$

From that point, an extended reactivity contrast $\mathcal{F} = \mathcal{A}\dfrac{d_f^\star}{d_m^\star}$ is defined. For a low reactivity contrast ($\mathcal{A} \approx 1$), $\mathcal{F}$ is close to 0.1. Then W accounts for $\dfrac{9}{2}\dfrac{\mathcal{F}}{\Sigma_m}$. Knowing that ξ_i satisfies Eq. 20 and that Eq. D.24c is an expression for $\dfrac{U}{\delta_a^2}$, ξ_i depends only on W:

$$\xi_i = 1 - \frac{1 - W + \sqrt{16 - 2W + W^2}}{5} \tag{D.27}$$

As displayed on Fig. D.3, for a fixed fibers volume fraction and a standard value for the reactivity contrast $\mathcal{F}$ equal to 0.1, ξ_i strongly decreases with the matrix volume fraction.

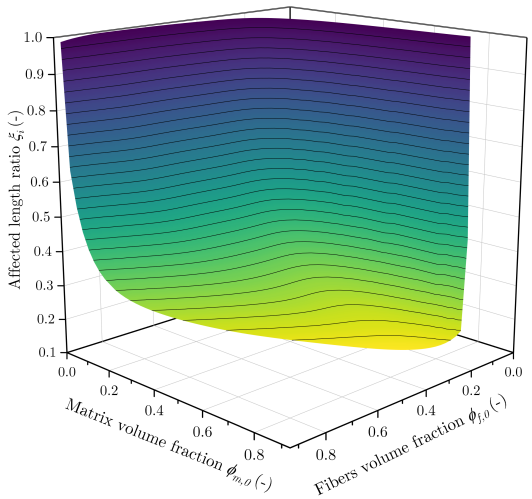

Figure D.3: Evolution of ξ_i in the $\{\phi_{f,0}; \phi_{m,0}\}$ parameters space for $\mathcal{F}$ equal to 0.1. **color should be used for that figure.**

D.4. Details for the recession rate equation

From the combination of Eq. D.21a and making the assumption that $\upsilon_c^{-1} \gg 1$, an analytical relation for the recession rate v_r as a function of ξ_i and δ_a is determined:

$$v_r = \frac{2D_0}{\delta_a \eta_{lim}} \frac{1}{\upsilon_c^{-1}\xi_i + \frac{\Phi_0}{3\upsilon_m}(4 - \xi_i)} \tag{D.28}$$

E. ANSYS Fluent CFD modeling details

E.1. Simulation set up

A detailed description of the TGA reactor and an associated schematic were given in Section 2.1.2. A global scale CFD modeling of the reactor was adressed in 2D axi-symmetric based on the work of Zancanaro *et al.* [35]. The sample geometry was simplified as a cylinder displaying a geometrical surface equivalent to the one of a 6 mm edge length cube. The mesh is composed of more than 16,000 hexahedral cells and 17,000 nodes and refined close to sensitive zones such as the sample surface. The quality of all elementary cells is acceptable

with low distorsion. The commercial CFD software *Fluent 17.2* [56] was used to solve gas flow and reactant species distribution in the experimental setup.

E.2. Data processing method

The apparent geometrical reactivity of the sample surface k_{app} (m.s^{-1}), including the carbon stoechiometric factor, satisfies Eq. E.1:

$$\frac{dm}{dt} = -j_{\text{exp}}\ S_{\text{eff}} = -k_{\text{app}}\ S_{\text{eff}}\ C_{O_2}^{n}\ M_C \tag{E.1}$$

and might be considered as the reactivity of an effective surface S_{eff} generating an oxidative mass flow j_{exp} including diffusion effects in the sample.

The following assumptions are made:

- according to thermodynamical considerations [37], $\text{CO}_{(\text{g})}$ is more likely to be produced than $\text{CO}_{2(\text{g})}$ for temperatures above 800K. The reaction equation which is then considered for oxidation tests carried at temperatures equal and above 1173K is the following:

$$2C_{(s)} + O_{2(g)} \rightleftharpoons 2CO_{(g)} \tag{E.2}$$

- the consumed dioxygen rate, which is equal to j_{exp} according to Eq. E.2, is uniformly reported on the overall sample surface, and is used an apparent geometrical reactivity;
- multi-component diffusion is simplified into a global diffusion coefficient computed from the average of binary diffusion coefficients of O_2 in N_2, O_2 in CO, CO in N_2 and CO_2 in N_2. Associated diffusion coefficient data are from the classical correlation of Massman [45];
- in Eq. E.1, n is equal to 1 for the reasons detailed in Section 2.1.4 ;
- the boundary concentration C_b is averaged on the overall sample surface.

E.3. Binary dioxygen diffusion coefficients

The binary diffusion coefficient D_0 of O_2 in N_2 is computed from Massman [45] data for each temperature tested. Detailed values are condensed in Table 5.

F. Fibers cases details from Section 5.2

F.1. Evolutions of the affected length for the fibers

Fig. F.1 is an illustration of $\lambda_f^2 Sh_f$ for three specific kinetics cases. One can notice that the fibers related quantity behaves, quite logically, like the matrix related quantity divided by the extended reactivity contrast $\mathcal{F}$, as demonstrated by Eqs. 28a, 28b, 30a and 30b. The behavior of $\lambda_m^2 Sh_m$ and $\lambda_f^2 Sh_f$ only differ by their order of magnitude.

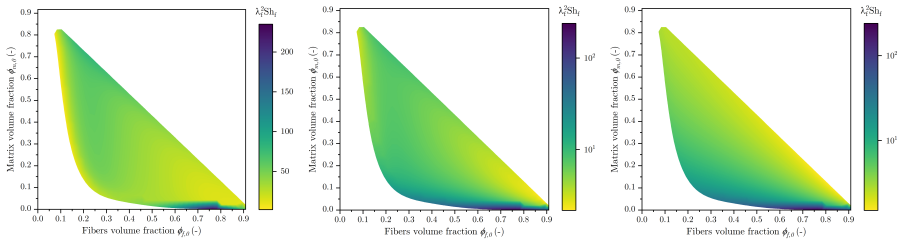

(a) $\mathcal{F} \ll 0.1$ (b) $\mathcal{F} = 0.1$ (c) $\mathcal{F} \gg 0.1$

Figure F.1: Graphs corresponding to Eq. 29 for three values of $\mathcal{F}$ in the $\{\phi_{f,0}; \phi_{m,0}\}$ parameter space. **color should be used for that figure.**

F.2. Effective reactivity for the fibers

Eq. 33 is illustrated by Fig. F.2. One can notice that the graphs from Fig. F.2 show similar evolutions as those from Fig. 14 with a proportionality factor of $\sqrt{A}\sqrt{\dfrac{d_f^\star}{d_m^\star}}\sqrt{\dfrac{\Omega_{s,f}}{\Omega_{s,m}}}$. In accordance with what has been said before, for increasing values of $\mathcal{F}$, the sensitivity of the material effective reactivity to its solid phases switches from the fibers to the matrix. However, in analogous domains of prevalence, the orders of magnitude of $\frac{Sh_c}{\sqrt{Sh_i}}$ are different which indicates that Sh_c is more dependent on $\sqrt{Sh_f}$ when fibers prevail than on $\sqrt{Sh_m}$ when matrix prevails. This confirms that the presence of fibers strongly reduces the composite effective reactivity when the matrix is the most reactive phase.

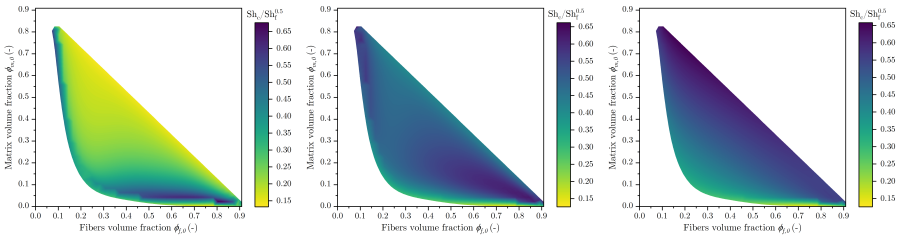

(a) $\mathcal{F} \ll 0.1$ (b) $\mathcal{F} = 0.1$ (c) $\mathcal{F} \gg 0.1$

Figure F.2: Graphs corresponding to Eq. 33 for three values of $\mathcal{F}$ in the $\{\phi_{f,0}; \phi_{m,0}\}$ parameter space. **color should be used for that figure.**

Nomenclature

Symbol	Meaning	Unit(s)
Greek symbols		
α	Diffusion exponent	-
γ	Condensed diffusion exponent	-
δ	Oxidation affected depth	m (or µm)
ε	Porosity	- (or %)
ε_p	Percolation porosity	- (or %)
$\varepsilon_{f,0}$	Fibrous architecture porosity	- (or %)
η_{lim}	Tortuosity	-
Θ	Thiele modulus	-
λ	Length ratio	-
ν_C	Carbon stoichiometric factor	-
ξ	Coordinate ratio	-
Ξ	Intermediate function (Eq. D.23)	-
ρ_s	Mass density	$g.cm^{-3}$
σ_v	Effective surface area	m^{-1}
Σ_m	Integrated matrix surface	-
υ	Condensation ratio	-
ϕ	Solid volume fraction	- (or %)
Φ_0	Structural dimensionless group	-
χ	Concentration ratio	-
Ω_s	Solid molar volume	$m^3.mol^{-1}$
Latin symbols		
$\mathcal{A}$	Reactivity contrast	-
A_i	Dimensionless group (Eqs. D.8a and D.8b)	-
A_e	Extinction angle	°
C	Molar concentration	$mol.m^{-3}$
$d^\star$	Characteristic length	m
D_0	Binary diffusion coefficient	$m^2.s^{-1}$
D_p	Effective diffusion coefficient	$m^2.s^{-1}$
E_a	Activation energy	$J.mol^{-1}$
$\mathcal{F}$	Extended reactivity contrast	-

$FWHM_D$	Full Width at Half Maximum of the D-band	cm^{-1}
$HWHM_G$	Half Width at Half Maximum of the G-band	cm^{-1}
I_D/I_G	Intensity ratio of the D- and G-bands	-
I_1	Prime integral (Eq. D.2)	$mol.m^{-3}$
j_{exp}	Experimental mass flow	$g.m^{-2}.s^{-1}$
j_{eff}	Analytical effective mass flow	$g.m^{-2}.s^{-1}$
k	Reaction activity	$m.s^{-1}$
k_{app}	Apparent geometrical reactivity	$m.s^{-1}$
k_{eff}	Material effective reactivity	$m.s^{-1}$
k_{het}	Heterogeneous reactivity	$m.s^{-1}$
k_0	Pre-exponential factor	$m.s^{-1}$
L_a	In-plane coherence length	nm
m	Mass	g
M_C	Carbon molar mass	$g.mol^{-1}$
n	Reaction partial order	-
P	Dimensionless group (Eq. D.5)	-
$\mathcal{P}$	Polynomial function (Eq. D.20)	-
$\dot{r}_{\text{exp}}$	Experimental recession rate	$\mu m.s^{-1}$
r_f	Fiber radius	m
$\mathcal{R}$	Universal ideal gas constant	$J.mol^{-1}.K^{-1}$
S	Surface	m^2
Sh	Sherwood number	-
t	Time	s
T	Temperature	K
v_r	Analytical recession rate	$m.s^{-1}$ (or $\mu m.s^{-1}$)
U	Parameter from Eq. D.24b	-
V	Parameter from Eq. D.24a	-
W	Parameter from Eq. 23b	-
x	Cartesian space coordinate	m
Subscripts and superscripts		
$_a$	Relative to overall material	
$_b$	Relative to the effective surface gas-solid boundary	
$_c$	Relative to the composite	
$_{CO}$	Relative to the production of $CO_{(g)}$	
$_{\text{eff}}$	Relative to the effective (*i.e.* geometrical) surface	
$_f$	Relative to the fibers	
$_i$	Relative to the interface fiber/matrix	
$_m$	Relative to the matrix	
$_s$	Relative to solid phase	
$_{\text{vol}}$	Relative to the internal surface	
$_0$	Relative to initial state	

Acknowledgments

This work was financially supported by ArianeGroup SAS through a PhD grant to Marina Fradin. The authors wish to thank Olivier Caty (Bordeaux INP, LCTS) for helping in 3D-image acquisition. X-ray µCT scans were obtained at the *Placamat* characterization service unit of Bordeaux University and CNRS.

References

[1] G. Savage, Carbon-Carbon Composites, Springer Netherlands, Dordrecht, 1993. doi:10.1007/978-94-011-1586-5.

[2] E. Fitzer, L. M. Manocha, Carbon Reinforcements and Carbon/Carbon Composites, Springer, 1998. doi:10.1007/978-3-642-58745-0.

[3] R. Weiß, Carbon/Carbons and Their Industrial Applications, WILEY-VCH Verlag GmbH, 2008, Ch. 4, pp. 69–111. doi:10.1002/9783527622412.ch4.

[4] H. Hatta, R. Weiß, P. David, Carbon/carbons and their industrial applications, in: N. P. Bansal, J. Lamon (Eds.), Ceramic Matrix Composites : Materials, Modeling and Technology, John Wiley & Sons, Ltd, Ch. 5, pp. 85–146. doi:10.1002/9781118832998.ch5.

[5] I. W. Smith, The intrinsic reactivity of carbons to oxygen, Fuel (1978). doi:10.1016/0016-2361(78)90055-8.

[6] E. Duvivier, Cinétique d'oxydation d'un composite Carbone/Carbone et influence sur le comportement mécanique, Ph.D. thesis, Bordeaux (1997). URL https://www.theses.fr/1997BOR10539

[7] C. Levet, B. Helber, J. Couzi, J. Mathiaud, J.-B. Gouriet, O. Chazot, et al., Microstructure and gas-surface interaction studies of a 3D carbon/carbon composite in atmospheric entry plasma, Carbon 114 (2017) 84–97. doi:10.1016/j.carbon.2016.11.054.

[8] C. Levet, J. Lachaud, V. Ducamp, R. Memes, J. Couzi, J. Mathiaud, et al., High-flux sublimation of a 3D carbon/carbon composite: Surface roughness patterns, Carbon 173 (2021) 817–831. doi:https://doi.org/10.1016/j.carbon.2020.11.023.

[9] G. L. Vignoles, J. Lachaud, Y. Aspa, Environmental Effects: Ablation of C/C Materials-Surface Dynamics and Effective Reactivity, in: Ceramic

Matrix Composites, John Wiley & Sons, Inc., Hoboken, NJ, USA, 2014, Ch. 12, pp. 353–388. doi:10.1002/9781118832998.ch12.

[10] G. L. Vignoles, Y. Aspa, M. Quintard, Modelling of carbon-carbon composite ablation in rocket nozzles, Composites Science and Technology 70 (9) (2010) 1303–1311. doi:10.1016/j.compscitech.2010.04.002.
URL http://dx.doi.org/10.1016/j.compscitech.2010.04.002

[11] J. Lachaud, Y. Aspa, G. L. Vignoles, Analytical modeling of the steady state ablation of a 3D C/C composite, International Journal of Heat and Mass Transfer 51 (9-10) (2008) 2614–2627. doi:10.1016/j.ijheatmasstransfer.2008.01.008.

[12] G. Vignoles, J. Lachaud, Y. Aspa, M. Quintard, Effective surface recession laws for the physico-chemical ablation of C/C composite materials, Vol. 31, Daytona Beach, FL, 2010, pp. 351–360, Conference of Mechanical Properties and Performance of Engineering Ceramics and Composites V - 34th International Conference on Advanced Ceramics and Composites, ICACC'10. doi:10.1002/9780470944127.ch33.

[13] J. Lahaye, F. Louys, P. Ehrburger, The reactivity of carbon-carbon composites, Carbon 28 (1) (1990) 137–141. doi:10.1016/0008-6223(90)90104-7.

[14] T. L. Dhami, O. P. Bahl, L. M. Manocha, Influence of matrix precursor on the oxidation behavior of carbon-carbon composites, Carbon 31 (5) (1993) 751–756. doi:10.1016/0008-6223(93)90011-X.

[15] P. Ehrburger, F. Louys, J. Lahaye, The concept of active sites applied to the study of carbon reactivity, Carbon 27 (3) (1989) 389–393. doi:10.1016/0008-6223(89)90071-7.

[16] J. C. Ferguson, F. Panerai, J. Lachaud, N. N. Mansour, Theoretical study on the micro-scale oxidation of resin-infused carbon ablators, Carbon 121 (2017) 552–562. doi:10.1016/j.carbon.2017.06.013.

[17] J. Lachaud, N. Bertrand, G. L. Vignoles, G. Bourget, F. Rebillat, P. Weisbecker, A theoretical/experimental approach to the intrinsic oxidation reactivities of C/C composites and of their components, Carbon 45 (14) (2007) 2768–2776. doi:10.1016/j.carbon.2007.09.034.

[18] F. Panerai, A. Martin, N. N. Mansour, S. A. Sepka, J. Lachaud, Flow-tube oxidation experiments on the carbon preform of a phenolic-impregnated carbon ablator, Journal of Thermophysics and Heat Transfer 28 (2) (2014) 181–190. doi:10.2514/1.T4265.

[19] J. C. Ferguson, F. Panerai, J. Lachaud, A. Martin, S. C. Bailey, N. N. Mansour, Modeling the oxidation of low-density carbon fiber material based on micro-tomography, Carbon 96 (2016) 57–65. doi:10.1016/j.carbon.2015.08.113.

[20] G. L. Vignoles, A. Turchi, D. Bianchi, P. Blaineau, X. Lamboley, D. Le Quang Huy, C. Levet, O. Caty, O. Chazot, Ablative and catalytic behavior of carbon-based porous thermal protection materials in nitrogen plasmas, Carbon 134 (2018) 376–390. doi:10.1016/j.carbon.2018.03.087.

[21] D. Kopeliovich, 5 - Advances in manufacture of ceramic matrix composites by infiltration techniques, in: I. Low (Ed.), Advances in Ceramic Matrix Composites, second edition Edition, Woodhead Publishing Series in Composites Science and Engineering, Woodhead Publishing, 2018, pp. 93–119. doi:https://doi.org/10.1016/B978-0-08-102166-8.00005-0.

[22] F. Langlais, G. Vignoles, 5.4 Chemical Vapor Infiltration Processing of Ceramic Matrix Composites (2018) 86–129.

[23] G. Vignoles, 8 - Chemical Vapor Deposition/Infiltration Processes for Ceramic Composites, in: P. Boisse (Ed.), Advances in Composites Manufacturing and Process Design, Woodhead Publishing, 2015, pp. 147–176. doi:https://doi.org/10.1016/B978-1-78242-307-2.00008-7.

[24] Y. Xu, Chemical Vapour Infiltration, Springer London, London, 2010, pp. 165–213. doi:10.1007/978-1-84882-894-0_5.

[25] I. Golecki, Rapid vapor-phase densification of refractory composites, Materials Science and Engineering: R: Reports 20 (2) (1997) 37–124, r20. doi:https://doi.org/10.1016/S0927-796X(97)00003-X.

[26] E. Frank, L. M. Steudle, D. Ingildeev, J. M. Spörl, M. R. Buchmeiser, Carbon fibers: Precursor systems, processing, structure, and properties, Angewandte Chemie - International Edition 53 (21) (2014) 5262–5298. doi:10.1002/anie.201306129.

[27] A. Lacombe, M. Lacoste, T. Pichon, 3D Novoltex® and Naxeco® carbon-carbon nozzle extensions; matured, industrial and available technologies to reduce programmatic and technical risks and to increase performance of launcher upper stage engines, 44th AIAA/ASME/SAE/ASEE Joint Propulsion Conference and Exhibit (July) (2008) 1–10. doi:10.2514/6.2008-5236.

[28] A. Lacombe, T. Pichon, J. M. Amouroux, HERAKLES thermal-structural composite materials boost rocket nozzle performance, 49th AIAA/ASME/SAE/ASEE Joint Propulsion Conference 1 PartF (July) (2013). doi:10.2514/6.2013-3863.

[29] A. P. Gillard, G. Couégnat, O. Caty, A. Allemand, P. Weisbecker, G. L. Vignoles, A quantitative, space-resolved method for optical anisotropy estimation in bulk carbons, Carbon 91 (2015) 423–435. doi:10.1016/j.carbon.2015.05.005.

[30] P. Lespade, A. Marchand, M. Couzi, F. Cruege, Caractérisation de matériaux carbonés par microspectrométrie Raman, Carbon 22 (4-5) (1984) 375–385. doi:10.1016/0008-6223(84)90009-5.

[31] J. M. Vallerot, X. Bourrat, A. Mouchon, G. Chollon, Quantitative structural and textural assessment of laminar pyrocarbons through Raman spec-

troscopy, electron diffraction and few other techniques, Carbon 44 (9) (2006) 1833–1844. doi:10.1016/j.carbon.2005.12.029.

[32] G. L. Vignoles, P. Weisbecker, J.-M. Leyssale, S. Jouannigot, G. Chollon, Carbones pyrolytiques ou pyrocarbones : des matériaux multiéchelles et multiperformances, Techniques de l'ingénieur 33 (2015). doi:10.51257/a-v1-nm3150.

[33] P. Mallet-Ladeira, P. Puech, C. Toulouse, M. Cazayous, N. Ratel-Ramond, P. Weisbecker, et al., A Raman study to obtain crystallite size of carbon materials: A better alternative to the Tuinstra-Koenig law, Carbon 80 (1) (2014) 629–639. doi:10.1016/j.carbon.2014.09.006.

[34] G. Dupupet, Fibres de carbone, Techniques de l'ingénieur TIB625. (am5134) (2008) 19. doi:10.51257/a-v1-am5134.

[35] M. Zancanaro, N. Bertrand, F. Rebillat, Definition of Optimized Conditions to Extract Accurate Kinetic Laws from TGA Experiments: Modeling and Validation, Oxidation of Metals 87 (3-4) (2017) 393–402. doi:10.1007/s11085-017-9716-6.

[36] J. Schindelin, I. Arganda-Carreras, E. Frise, V. Kaynig, M. Longair, T. Pietzsch, et al., Fiji: An open-source platform for biological-image analysis, Nature methods 9 (2012) 676–82. doi:10.1038/nmeth.2019.

[37] J. R. Arthur, Reactions between carbon and oxygen, Transactions of the Faraday Society 47 (1950) 164–178. doi:10.1039/tf9514700164.

[38] H.-W. Chang, R. M. Rusnak, Oxidation behavior of carbon-carbon composites, Carbon 17 (5) (1979) 407–410. doi:10.1016/0008-6223(79)90056-3.

[39] B. Dačić, S. Marinković, Kinetics of air oxidation of unidirectional carbon fibres/ CVD carbon composites, Carbon 25 (3) (1987) 409–415. doi:10.1016/0008-6223(87)90012-1.

[40] W. Guo, H. Xiao, E. Yasuda, Y. Cheng, Oxidation kinetics and mechanisms of a 2D-C/C composite, Carbon 44 (15) (2006) 3269–3276. doi:10.1016/j.carbon.2006.06.027.

[41] O. Coindreau, G. Vignoles, Assessment of geometrical and transport properties of a fibrous C/C composite preform using X-ray computerized microtomography: Part I. Image acquisition and geometrical properties, Journal of Materials Research 20 (9) (2005) 2328–2339. doi:{10.1557/JMR.2005.0311}.

[42] G. L. Vignoles, Reactive processes in high temperature porous materials, in: Porous media interaction with high temperature and high speed flows, no. STO-AVT-261 in von Karman Institute NATO Lecture Series.
URL https://www.vki.ac.be/index.php/events-ls/events/eventdetail/361/-/porous-media-interaction-with-high-temperature-and-high-speed-flows-s

[43] C. Charles, C. Descamps, G. L. Vignoles, Low pressure gas transfer in fibrous media with progressive infiltration: correlation between different transfer modes, International Journal of Heat and Mass Transfer 182 (2022) 121954. doi:10.1016/j.ijheatmasstransfer.2021.121954.

[44] C. Charles, Relations entre la structure de milieux fibreux et leurs propriétés thermiques et de transfert de masse, Ph.D. thesis, Université de Bordeaux (2022).
URL https://www.theses.fr/2021BORD0322

[45] W. J. Massman, A review of the molecular diffusivities of H2O, CO2, CH4, CO, O3, SO2, NH3, N2O, NO, and NO2 in air, O2 and N2 near STP, Atmospheric Environment 32 (6) (1998) 1111–1127. doi:10.1016/S1352-2310(97)00391-9.

[46] M. C. Halbig, J. D. McGuffin-Cawley, A. J. Eckel, D. N. Brewer, Oxidation kinetics and stress effects for the oxidation of continuous carbon fibers within a microcracked C/SiC ceramic matrix composite, Journal of

the American Ceramic Society 91 (2) (2008) 519–526. doi:10.1111/j.1551-2916.2007.02170.x.

[47] A. V. Govorov, A. A. Galiguzov, N. A. Tikhonov, A. P. Malakho, A. D. Rogozin, Study of Different Types of Carbon Fiber Oxidation Kinetics, Refractories and Industrial Ceramics 56 (6) (2016) 605–609. doi:10.1007/s11148-016-9897-6.

[48] X. Bertran, G. Chollon, J. Dentzer, R. Gadiou, S. Fouquet, M. A. Dourges, F. Rebillat, Oxidation behavior at moderate temperature under dry and wet air of phenolic resin-derived carbon, Thermochimica Acta 649 (2017) 13–21. doi:10.1016/j.tca.2016.12.013.

[49] R. Luo, J. Cheng, T. Wang, Oxidation behavior and protection of carbon/carbon composites prepared using rapid directional diffused CVI techniques, Carbon 40 (11) (2002) 1965–1972. doi:10.1016/S0008-6223(02)00025-8.

[50] X. Bertran, Comportement en milieu oxydant d'un composite carbone/carbone pour applications structurales entre 150 et 400°C dans l'aéronautique civile, Ph.D. thesis, Université de Bordeaux (2013).
URL https://www.theses.fr/175664196

[51] X. Bertran, C. Labrugère, M. A. Dourges, F. Rebillat, Oxidation behavior of PAN-based carbon fibers and the effect on mechanical properties, Oxidation of Metals 80 (3-4) (2013) 299–309. doi:10.1007/s11085-013-9388-9.

[52] M. Fradin, G. L. Vignoles, C. Ville, G. Couégnat, M. Ridard, F. Rebillat, Oxidation kinetics of a rough laminar pyrocarbon in O2-, H2O- and CO2-containing atmospheres, Corrosion Science (submitted) (2023).

[53] F. Lamouroux, X. Bourrat, R. Naslain, J. Sevely, Structure / Oxidation behavior relationship in the carbonaceous constituents of 2D-C / PyC / SiC composites, Carbon 31 (8) (1993) 1273–1288. doi:10.1016/0008-6223(93)90086-P.

[54] L. R. Zhao, B. Z. Jang, The oxidation behaviour of low-temperature heat-treated carbon fibres, Journal of Materials Science 32 (11) (1997) 2811–2819. doi:10.1023/A:1018612214572.

[55] F. Qin, L. Na Peng, G. Qiang He, J. Li, Y. Yan, Oxidation kinetics and mechanisms of carbon/carbon composites and their components in water vapour at high temperatures, Corrosion Science 90 (2015) 340–346. doi:10.1016/j.corsci.2014.10.027.

[56] ANSYS, ANSYS Fluent - CFD Software — ANSYS (2016).
URL http://www.ansys.com/products/fluids/ansys-fluent